Publication Year	2016
Acceptance in OA	2020-07-02T15:18:31Z
Title	Infrared High-resolution Integrated Light Spectral Analyses of M31 Globular Clusters from APOGEE
Authors	Sakari, Charli M., Shetrone, Matthew D., Schiavon, Ricardo P., Bizyaev, Dmitry, Allende Prieto, Carlos, Beers, Timothy C., Caldwell, Nelson, García-Hernández, D. A., LUCATELLO, Sara, Majewski, Steven, O'Connell, Robert W., Pan, Kaike, Strader, Jay
Publisher's version (DOI)	10.3847/0004-637X/829/2/116
Handle	http://hdl.handle.net/20.500.12386/26295
Journal	THE ASTROPHYSICAL JOURNAL
Volume	829

The Astrophysical Journal, 829:116 (23pp), 2016 October 1 doi:10.3847/0004-637X/829/2/116

INFRARED HIGH-RESOLUTION INTEGRATED LIGHT SPECTRAL ANALYSES OF M31 GLOBULAR CLUSTERS FROM APOGEE

Charli M. Sakari[1], Matthew D. Shetrone[2], Ricardo P. Schiavon[3,4], Dmitry Bizyaev[5,6,7], Carlos Allende Prieto[8,9], Timothy C. Beers[10], Nelson Caldwell[11], Domingo Aníbal García-Hernández[8,9], Sara Lucatello[12], Steven Majewski[13], Robert W. O'Connell[13], Kaike Pan[5], and Jay Strader[14]

[1] Department of Astronomy, University of Washington, Seattle WA 98195-1580, USA; sakaricm@u.washington.edu
[2] McDonald Observatory, University of Texas at Austin, HC75 Box 1337-MCD, Fort Davis, TX 79734, USA
[3] Gemini Observatory, 670 N. A'Ohoku Place, Hilo, HI 96720, USA
[4] Astrophysics Research Institute, Liverpool John Moores University, 146 Brownlow Hill, Liverpool, L3 5RF, UK
[5] Apache Point Observatory and New Mexico State University, P.O. Box 59, Sunspot, NM, 88349-0059, USA
[6] Special Astrophysical Observatory of the Russian AS, Nizhnij Arkhyz, Russia
[7] Sternberg Astronomical Institute, Moscow State University, Universitetsky prosp. 13, Moscow, Russia
[8] Instituto de Astrofísica de Canarias (IAC), Va Lactea s/n, E-38205 La Laguna, Tenerife, Spain
[9] Departamento de Astrofísica, Universidad de La Laguna (ULL), E-38206 La Laguna, Tenerife, Spain
[10] Department of Physics and JINA Center for the Evolution of the Elements, University of Notre Dame, Notre Dame, IN 46556, USA
[11] Harvard-Smithsonian Center for Astrophysics, 60 Garden Street, Cambridge, MA 02138, USA
[12] INAF Osservatorio Astronomico di Padova, Vicolo dellOsservatorio 5, I-35122 Padova, Italy
[13] Dept. of Astronomy, University of Virginia, Charlottesville, VA 22904-4325, USA
[14] Department of Physics and Astronomy, Michigan State University, East Lansing, MI 48824, USA

Received 2016 May 17; revised 2016 July 3; accepted 2016 July 11; published 2016 September 28

ABSTRACT

Chemical abundances are presented for 25 M31 globular clusters (GCs), based on moderately high resolution ($R = 22{,}500$) H-band integrated light (IL) spectra from the Apache Point Observatory Galactic Evolution Experiment (APOGEE). Infrared (IR) spectra offer lines from new elements, lines of different strengths, and lines at higher excitation potentials compared to the optical. Integrated abundances of C, N, and O are derived from CO, CN, and OH molecular features, while Fe, Na, Mg, Al, Si, K, Ca, and Ti abundances are derived from atomic features. These abundances are compared to previous results from the optical, demonstrating the validity and value of IR IL analyses. The CNO abundances are consistent with typical tip of the red giant branch stellar abundances but are systematically offset from optical Lick index abundances. With a few exceptions, the other abundances agree between the optical and the IR within the 1σ uncertainties. The first integrated K abundances are also presented and demonstrate that K tracks the α elements. The combination of IR and optical abundances allows better determinations of GC properties and enables probes of the multiple populations in extragalactic GCs. In particular, the integrated effects of the Na/O anticorrelation can be directly examined for the first time.

Key words: galaxies: abundances – galaxies: evolution – galaxies: individual (M31) – galaxies: star clusters: general – globular clusters: general

Supporting material: machine-readable table

1. INTRODUCTION

Integrated light (IL) spectroscopy of globular clusters (GCs) provides valuable clues about the assembly histories of distant galaxies and their GC systems. An IL spectrum comes from an entire stellar population; integrated chemical abundances therefore represent flux-weighted averages from the individual stars observed in the IL spectrum. Despite the potential difficulties in modeling the underlying stellar populations, there are certain elements, spectral features, or wavelength regions that provide robust IL abundances (see, e.g., Schiavon et al. 2004; Sakari et al. 2013). Low- and medium-resolution ($R \lesssim 5000$) IL spectroscopy provides ages, metallicities, and abundances of the elements with the strongest spectral features (e.g., C, N, Mg; Caldwell et al. 2011; Schiavon et al. 2013), while higher-resolution spectroscopy provides higher-precision abundances of a wider variety of elements (including neutron-capture elements such as Ba and Eu in the optical; McWilliam & Bernstein 2008; Colucci et al. 2009, 2012; Sakari et al. 2015). Integrated light spectral observations have identified, among other things, possible metallicity bimodalities (Perrett et al. 2002, though Caldwell et al. 2011 find no bimodality) and metallicity gradients (e.g., Caldwell et al. 2011) in M31's GC population, chemically peculiar GCs in M31's outer halo that may have been accreted (Sakari et al. 2015), α deficiencies in distant GCs that are associated with dwarf galaxies (Puzia & Sharina 2008), and enhanced [α/Fe] ratios in metal-rich GCs associated with the early-type galaxy NGC 5128 (Colucci et al. 2013). Integrated light spectroscopy has also provided insight into the nature of GCs themselves, through comparisons with Milky Way (MW) GCs (Schiavon et al. 2012), detections of anomalous abundances indicative of multiple populations (e.g., Colucci et al. 2009, 2014, Sakari et al. 2015), and abundance correlations with cluster mass (Schiavon et al. 2013).

Though previous IL observations have typically been at optical wavelengths (~3000–9000 Å), high-resolution infrared (IR) IL spectroscopy is now possible thanks to recent advances in IR spectroscopy. In particular, the Apache Point Observatory Galactic Evolution Experiment (APOGEE) provides multi-object, high-resolution ($R = 22{,}500$) spectroscopy with coverage in the H band (from 1.51 to

1.69 μm); this wavelength coverage has some significant advantages for IL spectroscopy:

1. *Insensitivity to hot stars.* IL spectra are composed of light from all the stars in a stellar population, encompassing a wide range of luminosity and temperature. At blue wavelengths, contributions from hot horizontal branch (HB) stars complicate analyses (e.g., Schiavon et al. 2004; Sakari et al. 2014). Similarly, optical spectra are more sensitive to turnoff stars and therefore require estimates of GC age. IR spectra are likely to be sensitive only to the brightest red giant branch (RGB) and asymptotic giant branch (AGB) stars, simplifying IL analyses.
2. *Additional spectral lines.* The *H* band offers different spectral lines than the optical. In particular, strong molecular lines of CN, CO, and OH enable determinations of C, N, and O abundances (Smith et al. 2013). There are CN indices in the optical, though they are in the blue and may be too weak in metal-poor clusters (Schiavon et al. 2013). The *H* band also offers lines that are complementary to the optical, including additional Mg, Al, Si, Ca, and Ti lines. Stronger Al and Si lines can also be utilized in the IR than in the optical.
3. *Opportunities to probe multiple populations in GCs.* The well-established chemical variations in MW GCs (e.g., in Na/O and Mg/Al; Carretta et al. 2009b) have been inferred to exist in extragalactic GCs because of their IL abundance ratios, notably high [Na/Fe] (Colucci et al. 2014; Sakari et al. 2015). The *H* band offers detectable lines from elements that should vary within (at least some) GCs, including C, N, O, Mg, and Al. The ability to detect [O/Fe] and directly probe the Na/O anticorrelation makes the IR particularly valuable for extragalactic GC studies.

However, IR IL spectroscopy also suffers from some disadvantages compared to the optical:

1. *Line blending.* In metal-rich clusters, molecular features dominate the *H* band; as a result, abundances derived from lines in the *H* band are sensitive to the abundances of C, N, and O. This blending is especially significant in spectra whose lines are already blended as a result of the cluster velocity dispersion.
2. *Weak lines at low metallicity.* Many of the strong features in IL spectra become weaker in the more metal-poor GCs and may disappear entirely. For the most metal-poor clusters, *H*-band IL spectroscopy may therefore not provide abundances for as many elements as the more metal-rich GCs.
3. *Sensitivity to evolved stars.* As stated above, the *H* band is most sensitive to the brightest cluster RGB and AGB stars. The abundances are therefore sensitive to how the evolved AGB stars are modeled (in terms of the isochrones, the model atmospheres, the relative numbers of AGB stars, and stochastic sampling).
4. *Lack of iron lines.* The high-resolution IL analyses of unresolved GCs that were developed by McWilliam & Bernstein (2008), Colucci et al. (2009, 2011, 2014), and Sakari et al. (2013, 2015) rely on Fe I lines to determine the parameters of the underlying stellar population (specifically the age and metallicity of an appropriate isochrone). However, there are few sufficiently strong Fe lines in the *H* band (especially at low metallicities), and any detectable Fe lines may be blended with other features.

Though IR IL spectroscopy may not be as informative as optical IL spectroscopy on its own, it offers valuable information that complements the optical, provided that IL analysis techniques are viable in the *H* band. For highly reddened objects, the IR might also provide the only viable spectra for abundance analyses. This paper presents the first IR IL detailed abundance analyses of GCs, utilizing targets in M31. The IR abundances are compared to those derived from optical lines (similar to the individual stellar analysis of Smith et al. 2013). The targets cover a wide range in metallicity and have all had previous high-resolution, detailed IL abundance analyses in the optical. These *H*-band IL spectra were observed during an ancillary program of the APOGEE survey, as described in Section 2. The analysis techniques are introduced in Section 3; *H*-band abundances for 25 clusters are then presented (Section 4), along with new optical abundances for five GCs (Appendix). The comparisons are discussed in detail in Section 5 and particular emphasis is placed on the feasibility of future high-resolution IR IL analyses.

2. OBSERVATIONS AND DATA REDUCTION

The data presented in this paper are a subset of a larger sample of M31 GCs. The subset of GCs in this paper were targets in previous high-resolution optical spectroscopic analyses and therefore have reference abundances for comparisons with the *H* band. The high-resolution optical abundances from Colucci et al. (2009, 2014) are supplemented with new results for five GCs, as described in the Appendix.

2.1. Target Selection and Observations

M31 GCs were observed as part of an ancillary project in the APOGEE survey (see Zasowski et al. 2013). Confirmed GCs were selected from the optical sample of Caldwell et al. (2009); altogether, ~250 GCs were observed by APOGEE, all with $H < 15$ mag. Of the larger sample, only 25 are utilized for this paper's comparison with optical abundances: these 25 are some of the brightest targets. Table 1 shows that all targets in this paper have $H < 13.5$ mag.

H-band spectra (1.51–1.69 μm) of the target clusters were obtained with the moderately high resolution ($R = 22{,}500$; Wilson et al. 2010, 2012) APOGEE spectrograph on the 2.5 m Telescope at Apache Point Observatory (Gunn et al. 2006). APOGEE is a multi-object spectrograph, with 300 fibers placed on a variety of science and calibration targets (including the sky). The dispersed spectra are fed to three detectors, providing "blue," "green," and "red" coverage within the *H* band. The details of the observations can be found in Majewski et al. (2015) and Zasowski et al. (2013), including descriptions of the plates and fibers that were utilized for the observations.

These GCs were observed in the same manner as individual APOGEE stellar target. A single fiber was allocated for each cluster; the fiber diameter of 2″ is large enough to cover most of the clusters past their half-light radii (Galleti et al. 2009). Several of the targets in the larger sample are close to the center of M31 and are affected by light from M31's unresolved field stars. Based on examination of the flux and signal-to-noise ratio (S/N) of background fibers, the background subtraction is

Table 1
Target List

Cluster	R.A. (J2000)	Decl.	R_{proj} (kpc)	V	H	Observing Epoch[a]	# of Visits[b]	S/N[c]	v_{helio} km s^{-1}
B006-G058	00:40:26.5	+41:27:26.7	6.43	15.46	12.74	11, 13	10	24.94	-251.2 ± 0.5
B012-G064	00:40:32.5	+41:21:44.2	5.78	15.04	12.79	11, 13	10	22.70	-361.6 ± 0.5
B034-G096[d]	00:41:28.1	+40:53:49.6	6.05	15.47	12.61	11	7	23.65	-554.4 ± 0.5
B045-G108	00:41:43.1	+41:34:20.0	4.90	15.83	13.00	11, 13	10	17.02	-423.3 ± 0.8
B048-G110[e]	00:41:45.5	+41:13:30.6	2.59	16.51	13.38	11, 13	10	7.99	-228.9 ± 1.0
B063-G124	00:42:00.9	+41:29:09.5	3.49	15.73	12.22	11	3	34.34	-306.2 ± 0.5
B088-G150	00:42:21.1	+41:32:14.3	3.79	15.00	12.34	11	7	29.28	-489.6 ± 1.0
B110-G172[e]	00:42:33.1	+41:03:28.4	2.93	15.28	12.35	11	7	29.26	-236.7 ± 0.4
B163-G217	00:43:17.0	+41:27:44.9	3.00	15.04	11.84	11	7	46.43	-166.4 ± 0.3
B171-G222[d,f]	00:43:25.0	+41:15:37.1	1.77	15.28	12.24	11	10	24.03	-276.3 ± 0.6
B182-G233[d]	00:43:36.7	+41:08:12.2	2.88	15.43	12.52	11, 13	6	22.82	-358.3 ± 0.5
B193-G244	00:43:45.5	+41:36:57.5	5.41	15.33	12.23	11	11	32.22	-66.1 ± 0.3
B225-G280[d]	00:44:29.8	+41:21:36.6	4.67	14.15	11.23	11	11	65.72	-162.5 ± 0.3
B232-G286[d]	00:44:40.5	+41:15:01.4	4.97	15.65	13.35	11, 13	10	10.98	-196.1 ± 1.0
B235-G297[d]	00:44:57.9	+41:29:23.7	6.46	16.27	13.39	11, 13	10	10.69	-94.4 ± 1.0
B240-G302[d]	00:45:25.2	+41:06:23.8	7.24	15.18	12.89	11, 13	10	17.64	-54.4 ± 0.9
B311-G033[d]	00:39:33.8	+49:31:14.4	13.11	15.45	12.85	11, 13	10	17.66	-502.8 ± 1.0
B312-G035[d]	00:39:40.1	+40:57:02.3	9.02	15.52	12.85	11, 13	10	13.58	-177.7 ± 0.9
B381-G315[d]	00:46:06.6	+41:20:58.9	8.72	15.76	13.14	11, 13	10	10.13	-82.9 ± 1.0
B383-G318[d]	00:46:12.0	+41:19:43.2	8.92	15.30	12.84	11, 13	10	16.09	-233.6 ± 0.8
B384-G319[d]	00:46:21.9	+40:17:00.0	16.42	15.75	13.00	11, 13	10	19.98	-364.5 ± 0.8
B386-G322	00:46:27.0	+42:01:52.8	14.08	15.64	12.95	11	6	23.07	-399.8 ± 0.8
B403-G348	00:49:17.0	+41:35:08.2	17.34	16.22	13.47	11	6	16.09	-269.3 ± 0.8
B405-G351	00:49:39.8	+41:35:29.7	18.28	15.20	12.76	11	6	21.26	-165.5 ± 0.6
B472-D064	00:43:48.4	+41:26:53.0	3.67	15.19	12.69	11, 13	6	24.52	-120.6 ± 0.7

Notes.

[a] Clusters were observed in 2011 and/or 2013.

[b] Each visit is 66.6 minutes of integration.

[c] Signal-to-noise ratios (S/Ns) are per pixel and represent the median value across the entire spectral range. There are approximately 2.06 pixels per resolution element in the blue, 2.27 in the green, and 2.66 in the red.

[d] Some visits were affected by superpersistence (see text). The superpersistence regions are masked out, leading to lower S/N in the 1.51–1.62 μm region; some abundances are derived with unmasked spectra and have been flagged in subsequent tables.

[e] All visits were affected by superpersistence.

[f] A background galactic component was subtracted during data reduction.

Reference. Positions, projected distances from the center of M31, and magnitudes are from the Revised Bologna Catalog (Galleti et al. 2009).

estimated to only be important for targets within 9′ of the center of M31 (outside 9′ there is no detectable background signal). Only one cluster in this sample, B171, had a background component subtracted. For B171 and the other GCs within 9′ that are not included in this analysis, separate fibers were placed on background regions adjacent to the clusters. Because the fiber collision distance of 72″ prohibited simultaneous GC and background observations, two 3° SDSS plates were used to observe these clusters (Zasowski et al. 2013): one plate contained the GC fibers, while another had the background fibers displaced from the target centers by ∼10″. These background fibers were placed on smooth galactic components, based on the M31 near-IR maps from the Two Micron All-Sky Survey (Skrutskie et al. 2006). Clusters without dedicated background fibers were observed with both plates.

The first pair of SDSS GC plates was observed during 2011; one received three visits (where one visit = 66.6 minutes), while another received four. In 2013, one to two more visits were obtained (see Table 1). A significant number of GCs were observed in both the 2011 and 2013 campaigns. Table 1 also shows the S/N ratios of the final spectra: all range from 10 to 65 per pixel.

2.2. Data Reduction

The APOGEE data-reduction pipeline (Nidever et al. 2015) provides reduced and flux-calibrated single-epoch spectra (so-called “visits”), with estimates of the noise and bad-pixel masks. Unlike most of the optical range, H-band spectra are affected by the presence of strong sky lines in both emission and absorption. The APOGEE data-reduction pipeline flags these regions via bits set in the bad-pixel mask. The sensitivity to the previously accumulated signal in some regions of the APOGEE detectors (superpersistence; Nidever et al. 2015) makes some spectral ranges in certain fibers almost useless for analysis, especially for targets with low S/N (though note that even if a fiber was located in the superpersistence area, the red part of its spectrum is unaffected by this effect and is viable for further analysis). Fortunately, the main APOGEE pipeline flags out such regions as well.

The combined spectrum of an individual target comes from a weighted average of all available visits in 2011 and 2013. A visit’s weight is calculated individually in each pixel as a product of the inverse variance multiplied by the inverted mask. The latter is a binary mask, where any nonzero pixels in the original bad-pixel mask (from the data-reduction pipeline)

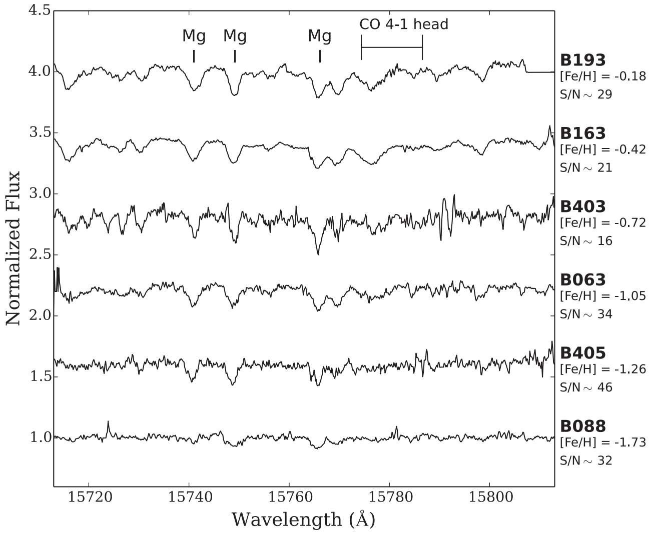

Figure 1. Sample *H*-band spectra of M31 GCs, spanning a range in metallicity (*H*-band [Fe/H] ratios are listed; see Section 4.1). Median S/N ratios (per pixel) are also given. The region around the strong Mg I lines and a CO band head is shown. Note that the line depths also depend on the velocity dispersion of the cluster.

have been set to zero, and any original pixels with no error bits have been set to one. Including this weight during the combination rejects all of the bad or problematic pixels from being included in the final spectrum. In particular, this will mask out regions affected by superpersistence. With regular APOGEE targets, the individual weighted visits for a given GC are then combined into a single, higher S/N spectrum, based on the radial velocity estimated for each individual visit. While this works well for typical, relatively bright APOGEE targets, most of the M31 GCs have mediocre to poor S/N (as low as S/N ∼ 10; see Table 1), and the radial velocity estimation is bypassed. Instead, the radial velocities are assumed to be constant between visits, and multiepoch spectra are aligned using barycentric correction information only. The pipeline therefore delivers the combined spectra, the associated errors, and the combined inverted mask.

As described in Section 2.1, special "background fibers" were reserved for clusters within 9′ of the center of M31 (only B171 in this paper's sample). The background fibers were treated as regular objects and were reduced and combined using the method described above. The galactic background light comes from an unresolved stellar population, and it is therefore assumed that any sharp spectral features are caused by noise or sky features; in order to avoid adding noise during the subtraction, the background spectra were smoothed by a Gaussian kernel with FWHM = 220 km s^{-1} to reproduce a mostly featureless background. The smoothed background was then subtracted from B171's spectrum.[15]

Samples of the final spectra are shown in Figure 1 for GCs with a range of metallicities. The region around the strong Mg I lines and a CO band head is shown. Note that the features are barely detectable at B088's metallicity and velocity dispersion.

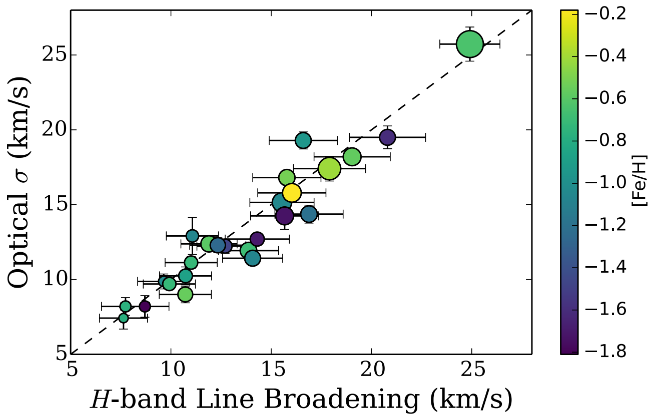

Figure 2. Comparison of *H*-band line broadening (with instrumental broadening removed) and optical velocity dispersion. The dashed line shows perfect agreement. The points are sized according to S/N ratios: the larger symbols have higher S/N, and are colored according to [Fe/H].

2.3. Radial Velocities and Line Broadening

The spectra for the metal-rich ([Fe/H] $\gtrsim -1.2$) GCs were shifted to the rest frame through cross-correlations with a spectrum of Arcturus (Hinkle et al. 2003) using the Image Reduction and Analysis Facility program (IRAF)[16] task *fxcor*. For metal-poor GCs with low S/N and very few detectable lines, this technique did not work; in this latter case, lines were identified and offsets were calculated manually. The final, heliocentric velocities are shown in Table 1 and are in excellent agreement with Colucci et al. (2014) and Caldwell et al. (2011).

Using spectrum syntheses to measure line strengths (see Section 3.1) requires modeling the line broadening due to (primarily) the GC velocity dispersion and the instrumental resolution. Although there are well-constrained velocity dispersions available from optical spectroscopy, the line-broadening values in the IR were determined by fitting the strong Si I lines at 15960 and 16095 Å. These lines were utilized instead of full-spectrum fitting in an attempt to minimize degeneracies between assumed initial abundances and line broadening. The precise broadening is more uncertain for the metal-poor GCs or GCs with lower S/N: high-S/N, metal-rich targets can have line-broadening uncertainties around ∼1 km s^{-1}, while lower S/N, metal-poor GCs can have uncertainties of ∼2–3 km s^{-1}. The abundance errors reflect uncertainties in fitting the full line profiles and therefore account for small uncertainties in the derived broadening values. Figure 2 shows a comparison between the line broadening derived from the *H* band (with the instrumental broadening removed) and the velocity dispersion from the optical, demonstrating that the two are in agreement. Note that the precise value for the velocity dispersion will depend upon the area of the cluster covered by the spectrograph slit or fiber. The optical values in Figure 2 were obtained from spectra with a slit size of 1.″7 × 7″ (Colucci et al. 2014) or a 3″ fiber (Appendix), while the APOGEE fibers have 2″ diameters.

---

[15] Note that for the optical B171 spectrum (Appendix) a separate background subtraction was not performed. Sky fibers were located 10″ from the central fiber, providing simultaneous sky observations. These sky fibers likely contained a background component as well.

[16] IRAF is distributed by the National Optical Astronomy Observatory, which is operated by the Association of Universities for Research in Astronomy, Inc., under cooperative agreement with the National Science Foundation.

3. ANALYSIS METHODS

H-band spectra exhibit strong molecular features as well as numerous atomic lines, particularly in metal-rich targets. This means that nearly every spectral feature is a blend of lines from multiple elements. In addition, IL spectral features are broadened by the GC velocity dispersion, exacerbating the blending problems. As a result, standard equivalent width analyses of individual features may not be suitable for abundance analyses of *H*-band IL spectra (see the discussions in Sakari et al. 2013 and Colucci et al. 2014). This paper therefore presents abundances that were derived from spectrum syntheses of the regions around each line of interest, utilizing a recent modification to the 2014 version of the line analysis code `MOOG` (Sneden 1973).

3.1. synpop: Spectrum Syntheses for Stellar Populations

`MOOG` (Sneden 1973) is a local thermodynamic equilibrium (LTE) line analysis code that has been widely used for individual stellar analyses, both in the optical and the IR. `MOOG`'s spectrum synthesis routine *synth* requires a model atmosphere and a line list; with this input, it then synthesizes a spectrum over the desired wavelength range, and abundances can be altered until the synthetic spectrum matches the observed one. `MOOG`'s *synpop* routine works the same way, but for an entire stellar population: given a list of model atmospheres (see Section 3.2) and a line list (Section 3.3), it produces a synthetic IL spectrum, weighted by the flux and number of stars assigned to each atmosphere. The *synpop* routine is therefore nearly identical to the synthesis version of the code `ILABUNDS` (McWilliam & Bernstein 2008; Sakari et al. 2013); however, *synpop* is now a supported part of `MOOG`, runs off current releases, and is publicly available.[17] This analysis utilizes the 2014 release of `MOOG`. As with the *synth* routine, *synpop* provides residual fits to identify the syntheses that best match the observed spectra.

3.2. Isochrones and Model Atmospheres

Since IL spectra contain contributions from all the stars in a stellar population, isochrones are used to model the underlying stellar populations in each GC. The BaSTI isochrones (Pietrinferni et al. 2004; Ferguson et al. 2005; Cordier et al. 2007) are utilized because they extend through the evolved HB and AGB phases; these are the same isochrones utilized for the comparison optical values. The ages and metallicities determined from the optical spectra (Colucci et al. 2014, Appendix A) are adopted; these values were found by minimizing trends in Fe I abundance with line wavelength, reduced equivalent width (REW), and excitation potential (EP; see McWilliam & Bernstein 2008) and agree reasonably well with the values derived from Lick indices (Caldwell et al. 2011). This procedure may not be suitable for *H*-band spectra; however, the *H*-band spectral lines are not as sensitive to cluster age (see Section 5.1). The standard HB morphologies from the BaSTI isochrones are adopted, along with extended AGBs. The effects of these choices are discussed in Colucci et al. (2009, 2012, 2014) and Sakari et al. (2014).

Once an appropriate isochrone has been identified, the isochrones are populated with stars to match the observed total magnitude for each GC, assuming a Kroupa (2002) initial mass function (IMF). The stars are binned along the isochrones, with each box containing 3.5% of the total flux. (Note that in the optical the box size has only a negligible effect on the abundances; Sakari et al. 2014.) Microturbulent velocities are assigned to each box based on an empirically motivated calibration with surface gravity (McWilliam & Bernstein 2008); this relation produces microturbulent velocities similar to the standard APOGEE relation (García-Pérez et al. 2015), except at very high and low surface gravities. Each box is then assigned a Kurucz model atmosphere[18] (Castelli & Kurucz 2004) with the average effective temperature, surface gravity, and microturbulence of the stars in that box. All atmospheres are chosen to be α-enhanced because optical integrated $[\alpha/\mathrm{Fe}]$ ratios are enhanced. This collection of model atmospheres is then fed as input to `MOOG`, along with a line list.

3.3. Line List

The line list adopted for this study includes both atomic and molecular species. The line list version adopted, linelist.20150714, is an updated version of what was used for DR12 results (Shetrone et al. 2015) and is the version adopted in DR13. Shetrone et al. (2015) noted a number of problems with the DR12 line list that have been corrected in the "linelist.20150714" version adopted here and documented in Holtzman et al. (in prep). A short summary of how the line list was generated including the differences with the DR12 version are detailed below.

The molecular line list is a compilation of literature sources including transitions of CO, OH, CN, C2, H2, and SiH. The CN line list was updated using a compilation from C. Sneden (2016, private communication). All molecular data are adopted without change, with the exception of a few obvious typographical corrections. The atomic line list was compiled from a number of literature sources and includes theoretical, astrophysical, and laboratory oscillator strength values. A few new lines were added from NIST[19] and other literature publications since the DR12 line list was created, including hyperfine splitting components for Al and Co. To calculate the astrophysical *gf* values, `Turbospectrum` was utilized (Alvarez & Plez 1998; Plez 2012) to generate synthetic spectra with varying oscillator strengths and damping values in order to fit the solar and Arcturus spectra. For lines with laboratory oscillator strengths, the astrophysical $\log(gf)$ values were not allowed to vary beyond twice the error quoted by the source.

One change from the methodology described in Shetrone et al. (2015) is that a different weighting scheme was used between the solar and Arcturus solutions. The astrophysical solutions were weighted according to line depth in Arcturus and in the Sun, which usually gives more weight to the Arcturus solution since the lines are generally stronger in the cooler, low surface gravity star, Arcturus, despite it being more metal-poor. Another difference from the methodology adopted in DR13 was the proper use of the center-of-disk spectral synthesis of the solar center-of-disk atlas using a microturbulence of 0.7 km s^{-1}.

---

[17] http://www.as.utexas.edu/~chris/moog.html

[18] http://kurucz.harvard.edu/grids.html

[19] http://physics.nist.gov/PhysRefData/ASD/lines_form.html

3.4. Abundance Determinations

As described in Section 3.1, the IR abundances are determined via spectrum syntheses. The best-fitting abundances were derived iteratively, following Smith et al. (2013). The procedure adopted for this analysis is as follows:

1. Adopt the best-fitting isochrones and model atmospheres from the optical (see Section 3.2).
2. Begin with standard abundance ratios for typical MW field stars at the same [Fe/H], e.g., $[\alpha/\mathrm{Fe}] = +0.4$ (Venn et al. 2004). Determine line-broadening parameters (see Section 2.3).
3. Determine initial values for the IR C, N, O, and Fe abundances based on syntheses of the lines in Smith et al. (2013). The fits are done by eye over a ~40 Å region, guided by the output residual fits in `MOOG`.
4. Iterate on the C, N, O, and Fe abundances until the values do not change. Adjust the isochrone [Fe/H], if needed, and reiterate on C, N, O, and Fe.
5. Find the abundances of the other elements.

Final [Fe/H] and [X/Fe] abundance ratios are calculated relative to the Asplund et al. (2009) solar abundances. All [X/Fe] ratios are calculated with the *H*-band [Fe I/H] abundance (since there are no detectable Fe II lines in the *H* band).

3.4.1. Strong Lines

McWilliam et al. (1995) showed that abundances derived from the strongest spectral lines are very sensitive to the treatment of the stellar atmosphere, particularly the outer layers. They estimated that lines with REWs[20] in the range $\mathrm{REW} > -4.7$ should be removed from abundance analyses, particularly when the Fe I lines are utilized to determine atmospheric parameters (or, in the case of IL analyses, the proper single stellar population parameters: age and metallicity). In the optical, lines with EWs larger than ~100–150 mÅ must be removed. In the *H* band, the REWs are smaller for lines of the same EW, and *H*-band analyses can safely utilize lines with strengths up to 300–320 mÅ. In some cases, when only strong lines are available for a given element, the REW limit was pushed up to −4.5; these lines may introduce offsets of ~0.1 dex (McWilliam et al. 1995), and these abundances have been flagged in all tables and figures. Similarly, some of the optical abundances were derived with strong lines, and those clusters are also flagged in all plots.

3.4.2. Abundance Errors

The random error in the abundance from each spectral line was estimated from the range of abundances that can fit the line profile, based on by-eye estimates and `MOOG`'s output residuals. Line profiles may not be perfectly fit due to, for example, S/N, uncertain continuum placement, telluric features, emission lines, or the adopted line broadening. Individual line abundance uncertainties range from 0.05 to 0.25 dex and are primarily driven by S/N. The uncertainty in a GC's mean abundance for a given element is determined by dividing the individual error by $\sqrt{N}$, where N is the number of lines for that element.

Potential systematic errors are more difficult to ascertain. Generally, the largest systematic uncertainties in IL analyses are due to uncertainties in modeling the underlying stellar populations, particularly the age of the population, the HB morphology, and the distribution of the brightest RGB and AGB stars (including the AGB/RGB star ratio). Sakari et al. (2014) present a detailed systematic error analysis for optical spectral lines, but those quantitative estimates may not apply to these IR lines. For instance, age and HB morphology can have strong effects in the optical (also see Colucci et al. 2014), but the effect in the *H* band seems to be negligible (see Section 5.1). The treatment of the brightest RGB and AGB stars is likely to have the largest effect in the *H* band. Section 5.3 demonstrates that the relative number of AGB stars, relative to RGB stars, is not likely to have a significant effect on the IL ratios; however, the choice of AGB models may affect some abundance ratios by as much as 0.2 dex (Sakari et al. 2014). Stochastic sampling of the upper RGB and AGB may also be significant; this will be examined in a separate paper. Systematic errors can also arise between analyses as a result of different models, assumptions, and techniques. Ultimately, systematic errors in the individual errors could be as high as 0.2 dex, though the errors in [X/Fe] ratios are likely to be smaller. However, the methodology, isochrones, model atmospheres, and solar abundances are the same between the high-resolution optical and IR analyses, which should reduce model-dependent systematic errors.

4. CHEMICAL ABUNDANCES

In this section, the *H*-band abundances are compared to (1) the high-resolution optical abundances from Colucci et al. (2009, 2014) and the Appendix and (2) the Lick index optical abundances from Schiavon et al. (2012, 2013).

4.1. Iron

Iron is a crucial element for chemical abundance analyses, since it is typically used to represent the GC metallicity. Table 2 shows the *H*-band Fe I abundances, along with the random errors and the number of measured lines. The clusters have been ordered from low to high [Fe/H]. Note that there are fewer measurable Fe I lines (2–13) in the *H* band compared to the optical (which has 20–60, depending on metallicity and wavelength range). The *H*-band Fe I lines are those quoted in Smith et al. (2013), along with several additional high-EP lines that were utilized for metal-poor stars by Lamb et al. (2015). Note that there are no useful Fe II lines in the *H* band. As mentioned in Section 3.4, the *H*-band Fe I abundances are mildly dependent on the adopted CNO abundances as a result of blending with CN and CO lines, particularly for the metal-rich targets.

Figure 3 compares the *H*-band [Fe I/H] abundances with the high-resolution optical [Fe I/H] ratios from Colucci et al. (2014) and the Appendix. Figure 3(a) compares the values to each other, while Figure 3(b) shows the differences versus *H*-band [Fe/H]. Though the *H*-band values are generally slightly higher than the optical (by 0.05 dex on average), all agree within the 1σ errors, and there is no trend with [Fe/H]. A small offset between the IR and optical [Fe I/H] may be expected due to NLTE effects (e.g., Kraft & Ivans 2003).

---

[20] $\mathrm{REW} = \log(\mathrm{EW}/\lambda)$, where EW is the equivalent width of a spectral line and λ is its wavelength; both are typically expressed in Å, and REW is dimensionless.

Table 2
Mean *H*-band Abundances and Random Errors: Fe, C, N, and O

	[Fe I/H]	*N*	[C/Fe][a]	*N*	[N/Fe][a]	*N*	[O/Fe][a]	*N*
B232	−1.81 ± 0.11	3	−0.20 ± 0.20	1	1.20 ± 0.20	1	0.22 ± 0.25	1
B088	−1.73 ± 0.07	6	−0.38 ± 0.07	5	1.31 ± 0.18	2	0.15 ± 0.08	4
B311	−1.70 ± 0.13	2	−0.03 ± 0.09	4	1.13 ± 0.14	2	0.35 ± 0.14	2
B012	−1.60 ± 0.10	5	−0.54 ± 0.15	5	0.93 ± 0.10	2	0.07 ± 0.10	4
B240	−1.48 ± 0.10	9	−0.36 ± 0.10	4	1.03 ± 0.11	3	0.31 ± 0.14	2
B405	−1.26 ± 0.07	9	−0.46 ± 0.08	5	0.93 ± 0.11	4	0.35 ± 0.09	2
B472	−1.20 ± 0.07	8	−0.41 ± 0.08	4	1.34 ± 0.09	4	0.26 ± 0.12	3
B386	−1.07 ± 0.14	4	−0.37 ± 0.04	4	1.16 ± 0.10	4	0.46 ± 0.03	3
B312	−1.06 ± 0.06	4	−0.48 ± 0.13	3	1.02 ± 0.19	2	0.35 ± 0.14	2
B063	−1.05 ± 0.09	12	−0.27 ± 0.09	5	1.30 ± 0.14	8	0.42 ± 0.07	5
B381	−1.03 ± 0.13	5	−0.28 ± 0.11	2	1.32 ± 0.14	2	0.32 ± 0.10	1
B182	−0.95 ± 0.06	6	−0.54 ± 0.08	5	1.09 ± 0.05	2	0.11 ± 0.05	3
B045	−0.88 ± 0.07	11	−0.41 ± 0.07	5	0.90 ± 0.10	4	0.33 ± 0.12	5
B048[b]	−0.78 ± 0.13	2	−0.17 ± 0.10	1	1.08 ± 0.12	3	0.53 ± 0.10	1
B235	−0.77 ± 0.06	8	−0.13 ± 0.10	4	1.21 ± 0.10	4	0.57 ± 0.08	3
B383	−0.72 ± 0.04	6	−0.18 ± 0.11	3	1.25 ± 0.10	3	0.47 ± 0.77	4
B403	−0.72 ± 0.09	9	−0.31 ± 0.08	4	1.06 ± 0.07	8	0.44 ± 0.11	4
B006	−0.69 ± 0.05	7	−0.32 ± 0.05	5	1.35 ± 0.04	6	0.32 ± 0.04	5
B225	−0.64 ± 0.05	10	−0.21 ± 0.05	4	1.09 ± 0.07	5	0.39 ± 0.09	4
B034	−0.60 ± 0.10	5	−0.24 ± 0.09	5	1.11 ± 0.07	7	0.45 ± 0.08	4
B110[b]	−0.57 ± 0.09	3	−0.32 ± 0.07	4	1.09 ± 0.12	6	0.33 ± 0.09	2
B384	−0.56 ± 0.04	11	−0.26 ± 0.07	5	1.11 ± 0.07	6	0.42 ± 0.05	4
B171	−0.52 ± 0.03	8	−0.28 ± 0.05	4	1.24 ± 0.04	8	0.36 ± 0.04	5
B163	−0.42 ± 0.09	12	−0.24 ± 0.05	5	0.94 ± 0.12	5	0.35 ± 0.08	4
B193	−0.18 ± 0.09	13	−0.10 ± 0.05	4	1.10 ± 0.09	7	0.45 ± 0.06	4

Notes.

[a] CNO abundances are determined from the CO, CN, and OH molecular lines in Smith et al. (2013), assuming $^{12}C/^{13}C = 6$ (see the text).

[b] The spectral range of this cluster is limited due to superpersistence; see Section 2.2.

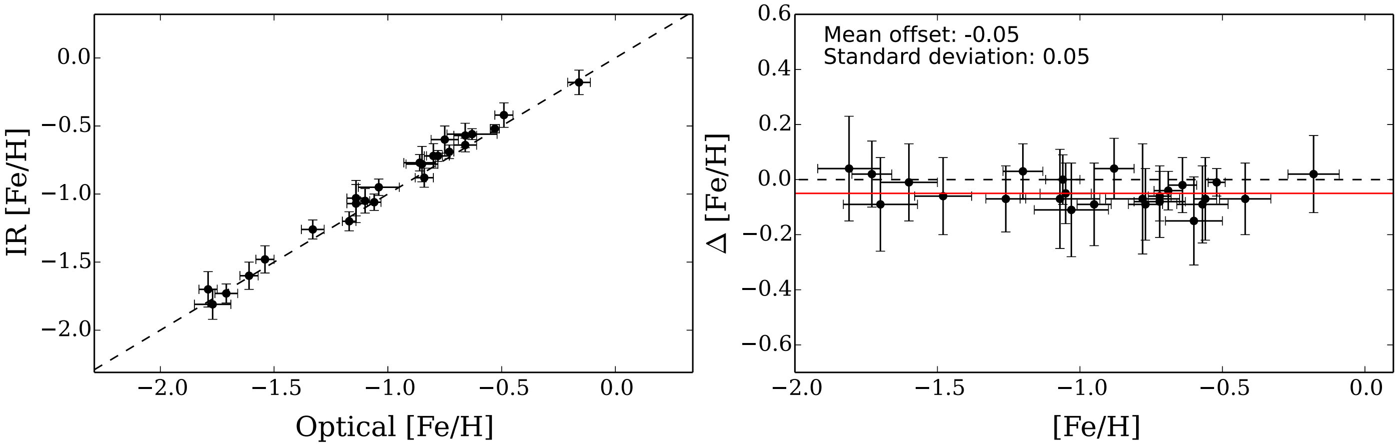

(a) (b)

Figure 3. Comparisons of the *H*-band [Fe I/H] abundances with the optical high-resolution abundances from the Appendix and Colucci et al. (2009, 2014). The error bars represent 1σ random errors, while the dashed lines show perfect agreement. Left: the two values plotted against each other. Right: the difference in [Fe I/H] (optical–IR) as a function of *H*-band [Fe/H]. The solid red line shows the average offset between the optical and *H* band, which is also quoted in the upper left corner.

Strong NLTE effects may plague the optical Fe I lines, especially in the brightest AGB stars (e.g., Lapenna et al. 2015), which would then affect the integrated Fe I lines. NLTE corrections to the Fe I lines in the *H* band are expected to be smaller than for those in the optical (García-Hernández et al. 2015), which could naturally lead to slight offsets between the optical and IR. Fe II is expected to be a more reliable Fe indicator. However, in the optical, there are fewer Fe II lines (1–16 for these GCs; Colucci et al. 2014), they are often weaker, most are located farther in the blue, and they are more sensitive to systematic uncertainties in the underlying stellar population (Sakari et al. 2014). For these reasons, the *H*-band Fe I abundances are not always in agreement with the optical Fe II, although the *average* offset is very small.

The small offset between the optical and *H*-band [Fe I/H] suggests that the NLTE offsets are likely to be small. The

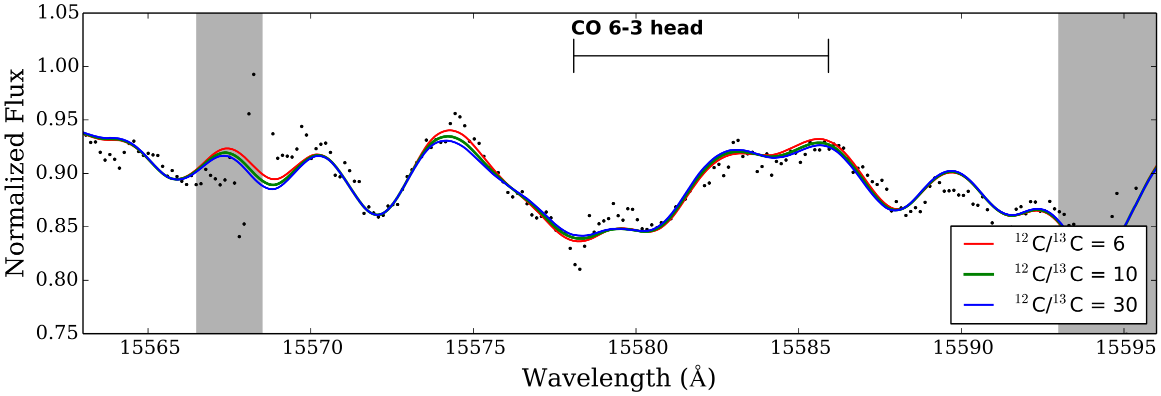

Figure 4. Sample syntheses of a C-sensitive CO feature in the most metal-rich GC, B193, demonstrating the small effects of the assumed $^{12}\mathrm{C}/^{13}\mathrm{C}$ ratio (the effects of varying $^{12}\mathrm{C}/^{13}\mathrm{C}$ are likely to be even smaller in more metal-poor GCs). The gray areas show regions that were masked out in the data-reduction pipeline (see Section 2.2). Three $^{12}\mathrm{C}/^{13}\mathrm{C}$ ratios are shown: 6, 10, and 30. Though the lower $^{12}\mathrm{C}/^{13}\mathrm{C}$ is slightly preferred, the differences are quite small.

H band therefore provides robust, integrated [Fe I/H] ratios down to at least [Fe/H] ~ −1.8, depending on S/N and GC velocity dispersion.

4.2. Light Elements: Carbon, Nitrogen, and Oxygen

Carbon, nitrogen, and oxygen are crucial elements for GC studies. In the *H* band, C, N, and O abundances can be determined from syntheses of CO, CN, and OH molecular lines (see Smith et al. 2013) with an assumed $^{12}\mathrm{C}/^{13}\mathrm{C}$ ratio. In these IL spectra, the S/N is not sufficient or the blending is too severe to measure a precise $^{12}\mathrm{C}/^{13}\mathrm{C}$ ratio (though in some cases it is evident that $^{12}\mathrm{C}/^{13}\mathrm{C} < 20$). For all clusters, $^{12}\mathrm{C}/^{13}\mathrm{C} = 6$ is adopted to represent the approximate value for stars at the tip of the RGB (e.g., Gratton et al. 2000). Since most of the molecular features are not strongly dependent on the precise $^{12}\mathrm{C}/^{13}\mathrm{C}$ ratio and the *H*-band IL spectrum is dominated by the tip of the RGB stars, this assumption should not have a strong effect on these IL abundances (see Figure 4). The final [C/Fe], [N/Fe], and [O/Fe] ratios are listed in Table 2, while sample syntheses of N-sensitive CN features are shown in Figure 5.

Figure 6 shows a comparison between the *H*-band and optical [C/Fe] and [N/Fe] ratios as a function of [Fe/H]. Reliable C, N, and O abundances can be difficult to obtain in the optical, particularly in IL spectra. C and N can be determined from CN and C_2 features in the blue (e.g., Worthey et al. 1994; Tripicco & Bell 1995; Schiavon 2007), but the exact abundances rely on an assumed O abundance (Graves & Schiavon 2008). O can be determined via the forbidden lines at 6300 and 6363 Å, but this requires high-resolution, high-S/N spectra of low velocity dispersion GCs because the lines are weak. The comparison optical values are therefore from the Lick index analyses of Schiavon et al. (2012, 2013) and are only available for metal-rich GCs ([Fe/H] $\gtrsim -1$). These [C/Fe] and [N/Fe] ratios are determined from the $C_2$4668 and CN_1 and CN_2 (~4140–4180 Å) Lick indices, assuming a fixed [O/Fe] = 0.3 for all GCs. Figure 6 demonstrates that, in general, the *H*-band [C/Fe] ratios are lower than the optical values by 0.2 dex, on average, while the [N/Fe] ratios are significantly higher (by 0.5 dex on average, when the three GCs in agreement are removed). The [N/Fe] ratios agree for the massive, metal-rich GCs B193, B163, and B225, though the [C/Fe] ratios are still slightly offset for the latter two. Note that the *H*-band abundances agree with the expected abundances for the tip of the RGB stars, which have dredged up products from CNO cycling (Gratton et al. 2000).

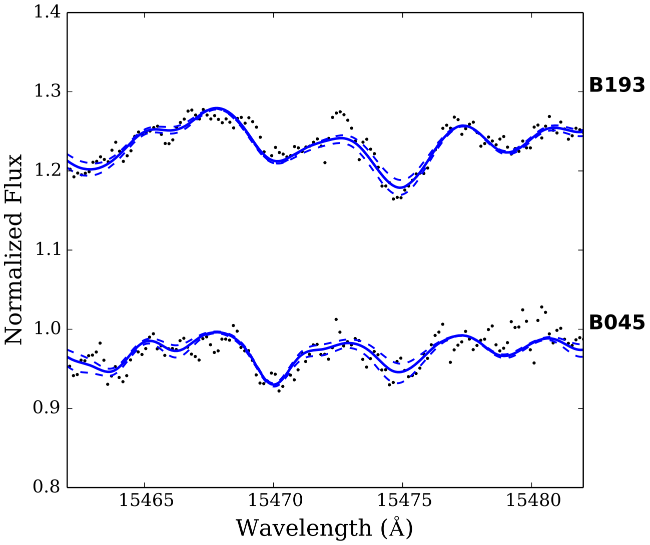

Figure 5. Sample syntheses of CN features in two GCs, B193 and B045; these features are used to determine [N/Fe]. The solid lines show the best-fit syntheses, while the dashed lines show $\pm 1\sigma$ uncertainties in [N/Fe] of 0.20 dex in both cases.

For the GCs with strong disagreement (i.e., all targets except the most metal-rich GCs), the optical Lick index CNO values do not fit the IR features. To demonstrate this, syntheses of a CO band head in B171, B006, and B045 are shown in Figure 7, with the optimal *H*-band CNO abundances and the Lick index C, N, and (assumed) O abundances. The 16183 Å CO band head is primarily sensitive to C; the syntheses in Figure 7 suggest that the Lick C abundances are too high to fit the *H*-band features, particularly for the more metal-poor GCs in the sample.

This disagreement between the optical and the *H* band is significant and will be addressed in Section 5.2.1.

4.3. Light Elements: Sodium, Magnesium, and Aluminum

The "light" elements Na, Mg, and Al are also important for GC studies because their abundances are known to vary

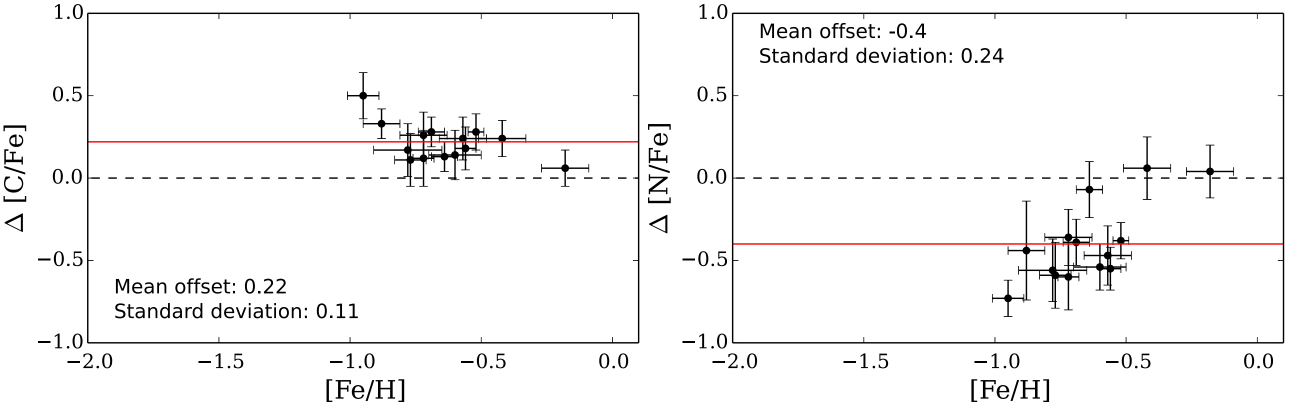

Figure 6. Comparisons of the *H*-band [C/Fe] (left) and [N/Fe] (right) ratios with the optical values from Schiavon et al. (2012, 2013) as a function of *H*-band [Fe/H]. The differences are given as optical–*H*-band. The error bars represent 1σ random errors, the dashed line shows perfect agreement, and the solid red line shows the average offset (which is quoted in each panel).

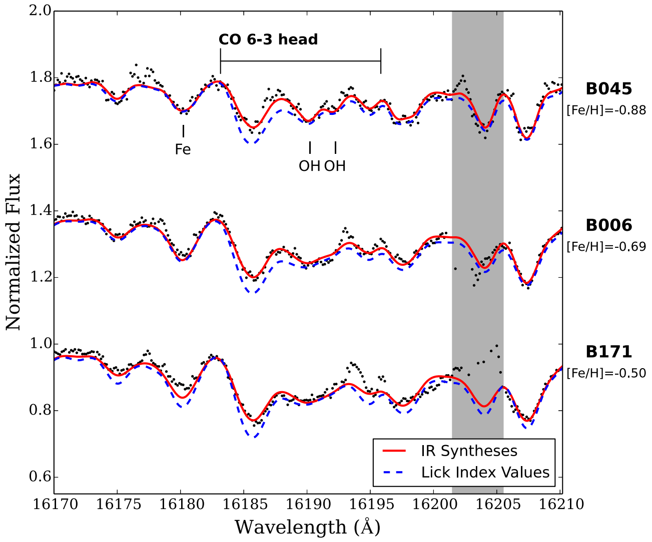

Figure 7. Syntheses of the 16183 Å CO band head, which is primarily sensitive to [C/Fe], in B171, B006, and B045. The gray area shows a region that was masked out in the data-reduction pipeline (see Section 2.2). The black points show the data, and the solid red lines show the best-fitting syntheses from this analysis. The dashed blue lines show syntheses with the optical Lick index [Fe/H], [C/Fe], [N/Fe], and (assumed) [O/Fe] ratios.

between stars within GCs (e.g., Carretta et al. 2009b). The *H* band offers lines complementary to the optical, with varying line strengths and EPs. While robust optical Na abundances can be derived from the 5682/5688 and 6154/6160 Å doublets (and possibly the NaD lines for metal-poor GCs), there is only one detectable weak doublet in the *H* band, which comes from a higher EP transition and is not detectable in the most metal-poor GCs. Mg has several medium-strength and strong lines in the optical; the *H* band offers two to six more. As mentioned in Section 3.4, stronger lines can be utilized in the IR, making the strong *H*-band Mg lines useful for GCs over a wide range of metallicities. Optical Al is primarily determined from the weak 6696/6698 Å lines, which are not detectable in the lowest-metallicity GCs (though there are additional lines in the blue and red). The *H* band offers two strong and one moderately strong Al lines, which can be detected even in low-metallicity GCs (note that these strong Al I lines have hyperfine structure components that must be included to properly reproduce the strengths of the lines). The strongest Al I line becomes prohibitively strong at moderate metallicity ([Fe/H] ∼ −1.2), while for the highest-metallicity clusters all three Al lines are too strong. For clusters with only strong lines, the REW limit was pushed up to −4.5; as discussed in Section 3.4.1, this may introduce systematic uncertainties of ∼0.1 dex.

The *H*-band Na, Mg, and Al abundances are shown in Table 3, while Figure 8 shows the optical versus *H*-band comparisons. There are few GCs with *H*-band and optical [Na/Fe] abundances (because the *H*-band lines are weak and difficult to detect). For the four GCs with both optical and *H*-band [Na/Fe] ratios, the agreement is decent. The *H* band also provides a [Na/Fe] abundance for B193, which was not available in the optical. Conversely, the weakness of the optical 6696/6698 Å lines means that there are only a few GCs with optical [Al/Fe] ratios. For those 10 GCs in common, the agreement between the optical and *H* band is generally good, though the errors are large and there is a large scatter. The *H*-band [Al/Fe] abundances are generally lower than the optical, with one exception: B045's [Al/Fe] does not agree with the optical value within its 1σ errors; its *H*-band value is ∼0.2 dex higher than its optical value.

Figure 8(c) shows that though the Mg abundances have a large scatter in the optical–*H*-band difference, this scatter is within the errors. One cluster, B193, has a larger optical [Mg/Fe] by ∼0.2 dex. However, this cluster's optical Mg abundance was derived with a single strong line (at 5528 Å); it is thus possible that the optical [Mg/Fe] is systematically offset by >0.1 dex (see the discussion in Section 3.4.1 and McWilliam et al. 1995). Systematically higher [Mg/Fe] ratios are also seen for the other metal-rich GCs whose Mg abundances were derived with the same strong line. Figure 8(d) compares these *H*-band Mg abundances to the lower-resolution Lick index values from Schiavon et al. (2013), for metal-rich clusters only; the Mg abundances agree within 1σ errors. One cluster, B403, has an optical Lick index [Mg/Fe] that is much higher than its *H*-band value, by ∼0.4 dex. However, this cluster's [Fe/H] is also in disagreement by >0.2 dex, so this offset in [Mg/Fe] is not likely to be significant.

Three clusters (B088, B240, and B235) have lower optical high-resolution Mg abundances (by 0.2–0.4 dex) than in the *H* band. For all three cases, both optical and *H*-band

Table 3
Mean *H*-band Abundances and Random Errors: Na, Mg, Al, Si, Ca, and Ti

	[Na/Fe]	N	[Mg/Fe]	N	[Al/Fe]	N	[Si/Fe]	N	[Ca/Fe]	N	[Ti/Fe]	N
B232	⋯	⋯	−0.01 ± 0.10	1	⋯	⋯	0.47 ± 0.10	1	⋯	⋯	⋯	⋯
B088	⋯	⋯	0.03 ± 0.10	3	0.51 ± 0.20	1	0.38 ± 0.09	3	0.31 ± 0.20	1	⋯	⋯
B311	⋯	⋯	−0.04 ± 0.14	2	⋯	⋯	0.21 ± 0.10	3	0.38 ± 0.40	1	⋯	⋯
B012	⋯	⋯	−0.14 ± 0.18	2	0.38 ± 0.15	1	0.43 ± 0.11	2	⋯	⋯	⋯	⋯
B240	⋯	⋯	0.20 ± 0.07	4	0.41 ± 0.15	2	0.22 ± 0.06	4	⋯	⋯	⋯	⋯
B405	⋯	⋯	0.07 ± 0.12	3	0.35 ± 0.20	1	0.35 ± 0.08	3	⋯	⋯	⋯	⋯
B472	⋯	⋯	0.14 ± 0.10	4	0.49 ± 0.20	1[a]	0.14 ± 0.16	5	0.32 ± 0.14	2	⋯	⋯
B386	⋯	⋯	0.06 ± 0.10	1	0.46 ± 0.08	1	0.46 ± 0.08	3	0.26 ± 0.20	1	0.36 ± 0.10	1
B312	⋯	⋯	−0.05 ± 0.20	1	0.35 ± 0.14	2	0.52 ± 0.07	3	⋯	⋯	⋯	⋯
B063	⋯	⋯	0.34 ± 0.08	3	0.29 ± 0.20	1	0.36 ± 0.08	3	0.49 ± 0.10	1	0.24 ± 0.08	3
B381	⋯	⋯	0.22 ± 0.10	1	0.47 ± 0.15	1	0.41 ± 0.05	4	0.22 ± 0.10	3	⋯	⋯
B182	⋯	⋯	0.19 ± 0.05	2	0.19 ± 0.11	2	0.46 ± 0.08	3	0.44 ± 0.07	2	0.34 ± 0.20	1
B045	⋯	⋯	0.22 ± 0.15	2	0.32 ± 0.15	1	0.43 ± 0.06	2	0.20 ± 0.13	2	0.27 ± 0.14	2
B048	⋯	⋯	⋯	⋯	⋯	⋯	0.48 ± 0.10	2	0.32 ± 0.07	2	⋯	⋯
B235	⋯	⋯	0.27 ± 0.13	2	0.39 ± 0.20	1	0.40 ± 0.05	4	0.37 ± 0.07	2	⋯	⋯
B383	⋯	⋯	0.22 ± 0.09	2	0.22 ± 0.14	2	0.35 ± 0.06	4	0.34 ± 0.07	2	⋯	⋯
B403	0.32 ± 0.20	1	0.05 ± 0.13	2	⋯	⋯	0.42 ± 0.10	1	0.22 ± 0.06	2	⋯	⋯
B006	0.39 ± 0.14	2	0.43 ± 0.05	2	0.43 ± 0.15	1[a]	0.37 ± 0.14	5	0.31 ± 0.07	2	0.43 ± 0.07	2
B225	⋯	⋯	0.24 ± 0.14	2	0.64 ± 0.14	2	0.32 ± 0.06	3	0.34 ± 0.06	3	0.39 ± 0.15	1
B034	⋯	⋯	0.30 ± 0.10	1	0.40 ± 0.20	1	0.35 ± 0.10	3	0.30 ± 0.07	2	0.35 ± 0.11	2
B110	⋯	⋯	0.23 ± 0.11	2	0.32 ± 0.14	1	0.31 ± 0.08	2	0.28 ± 0.07	2	⋯	⋯
B384	⋯	⋯	0.26 ± 0.13	2	0.16 ± 0.09	1	0.32 ± 0.09	4	0.23 ± 0.08	4	0.31 ± 0.11	2
B171	0.57 ± 0.20	1	0.37 ± 0.10	1	⋯	⋯	0.27 ± 0.08	5	0.30 ± 0.07	2	0.35 ± 0.10	2
B163	0.57 ± 0.10	1	0.22 ± 0.10	1	0.56 ± 0.05	2[a]	0.19 ± 0.09	3	0.27 ± 0.05	2	0.22 ± 0.10	1
B193	0.64 ± 0.05	2	0.19 ± 0.10	1	0.39 ± 0.20	1[a]	0.27 ± 0.10	3	0.34 ± 0.15	2	0.36 ± 0.08	3

Note.
[a] This *H*-band abundance was derived from at least one strong line with $-4.7 < \mathrm{REW}$ -4.5, which may lead to systematic uncertainties of ~0.1 dex (McWilliam et al. 1995).

abundances are derived from three to four lines, each of which gives consistent results. B235's *H*-band [Mg/Fe] agrees with the lower-resolution Lick index results from Schiavon et al. (2013); the other two were not included in that paper because they are too metal-poor. B088 is offset by 4σ according to the errors quoted in Colucci et al. (2014). However, these quoted optical errors are quite small (0.02 dex due to age uncertainties), suggesting that their stated error is too small. Even if a larger error of 0.1 dex is adopted for the optical, B088 is still offset by $>2\sigma$. This discrepancy will be investigated in Section 5.2.3.

4.4. Alpha Elements: Silicon, Calcium, and Titanium

The α elements Si, Ca, and Ti mainly form in massive stars and are expelled into the interstellar medium by core-collapse supernovae (which also produce iron). (Mg is also an α element; however, because it can vary between stars within a single GC, it is discussed in Section 4.3 with O, Na, and Al.) Type Ia supernovae from lower-mass stars also produce copious amounts of iron but very little α elements. The ratio of [α/Fe] therefore probes contributions from Type II versus Ia supernovae and is valuable for galactic chemical evolution studies. Because chemical evolution in dwarf galaxies proceeds differently than in massive galaxies, the chemical abundances of dwarf galaxy stars and clusters diverge with increasing metallicity (see, e.g., Tolstoy et al. 2009). The [α/Fe] ratios can therefore be used for chemical tagging of GCs (e.g., Hogg et al. 2016) and are essential for IL spectroscopy of extragalactic GCs (e.g., Colucci et al. 2012, 2014; Sakari et al. 2015).

Again, the *H* band provides lines complementary to the optical. The optical has numerous silicon lines, but they are often weak and difficult to detect in metal-poor GCs. There are three strong Si I lines in the *H* band and six more moderately strong lines. Note that the strongest Si I lines at 15960 and 16095 Å become too strong (REW $\gtrsim -4.7$) at high metallicity ([Fe/H] $\gtrsim -0.7$). The optical has many detectable Ca I lines of varying strength. Furthermore, these lines are also largely insensitive to uncertainties in the underlying stellar populations (e.g., the distribution of stars in temperature–log *g* space; Sakari et al. 2014). In the *H* band there are three Ca I lines at high EP, though two are extremely blended, leading to large random errors. Ti I and Ti II lines are readily available in the optical, but both suffer from potential systematic uncertainties. The Ti I lines may be affected by NLTE effects (Bergemann 2011) and are strongly affected by uncertainties in the underlying stellar populations (Sakari et al. 2014). The Ti II lines are also affected by uncertainties in the stellar populations, and many of the lines are located farther in the blue (where the S/N is often lower and where contributions from hotter stars may have a larger effect). The *H* band offers a handful of moderate-strength Ti I lines; though they are often blended with other features, these lines may be less affected by uncertainties in the underlying stellar populations.

The abundances of the α elements are listed in Table 3 and are compared with the optical abundances in Figure 9. Figure 9(a) compares [Si/Fe]. The uncertainties in the optical Si abundances can be quite large because the lines are often

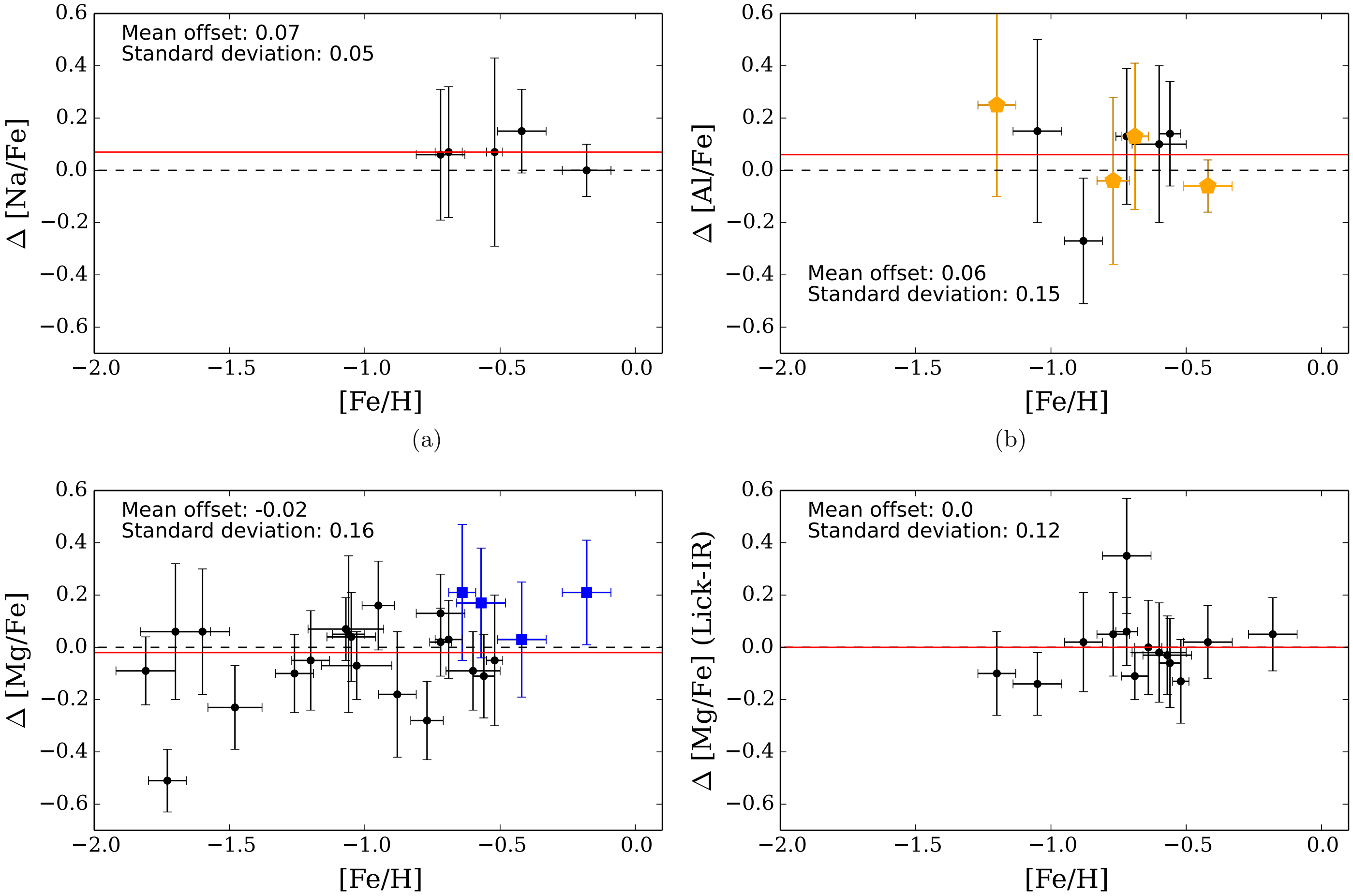

(a) (b)

(c) (d)

Figure 8. Comparisons of the *H*-band [Na/Fe] (top left), [Al/Fe] (top right), and [Mg/Fe] (bottom left) with the optical values from Colucci et al. (2014) and the Appendix as a function of *H*-band [Fe/H]. The bottom right shows a comparison of *H*-band [Mg/Fe] with the Lick index [Mg/Fe] from Schiavon et al. (2013). Differences are optical–*H*-band. The error bars represent 1σ random errors, the dashed lines show perfect agreement, the solid red lines show the average offsets, and the quoted values list the average offsets. Clusters whose optical abundances are derived from very strong lines are shown with blue squares, while clusters whose infrared abundances are derived from strong lines are shown with orange pentagons.

weak. There are three GCs whose [Si/Fe] ratios do not agree between the optical and the *H* band within 1σ errors: B403, B381, and B240, all of which have optical [Si/Fe] ratios that are >0.5 dex. The stronger *H*-band Si lines may produce higher-precision Si abundances compared to the weaker optical Si lines.

Calcium is an element that can be difficult to detect in the *H* band, particularly in the most metal-poor GCs. The four available lines are from high-EP transitions that are clumped together in a region at ~16150 Å that is affected by superpersistence in some visits (see Table 1). The optical abundances, however, are well constrained from measurements of 2–13 lines. When *H*-band Ca lines can be detected, Figure 9(b) shows that the agreement between the optical and the *H* band is generally good, with the exception of B034 and B235, whose *H*-band [Ca/Fe] ratios are $>1\sigma$ higher than the optical values.

The *H*-band Ti I lines are very weak and blended in these spectra. Table 3 shows that Ti is not detectable in most metal-poor clusters and is difficult to detect in GCs with high velocity dispersions. For the GCs with measurements in both the *H* band and the optical, the *H*-band [Ti I/Fe I] ratios are generally higher than the optical values, as seen in Figure 9(c). B006, B034, and B193 are not in agreement; however, all GCs show agreement between *H*-band [Ti I/Fe I] and optical [Ti II/Fe II] (Figure 9(d)). This suggests that the optical Ti I lines are systematically affected in some way that the IR lines are not. Again, this could indicate that the *H*-band lines are less affected by NLTE effects (e.g., García-Hernández et al. 2015).

4.5. Potassium

The *H* band offers two moderate-EP (2.67 eV) K I lines at 15163 and 15168 Å. These lines lie on the blue edge of APOGEE's spectral range, and they are not easily detectable in most of the targets with low S/N. K *is* detectable in only a handful of the GCs, as shown in Table 4. There are no optical IL K abundances to compare with, but [K/Fe] can be compared to the α elements. Potassium is not an α element, yet abundance analyses of stars in the MW indicate that the chemical evolution of [K/Fe] is similar to the evolution in [α/Fe] (see, e.g., Zhang et al. 2006). The [K/Fe] ratios are compared to the optical [Ca/Fe] ratios in Figure 10; the agreement is generally quite good. The optical [Ca/Fe] ratios are chosen for this comparison in lieu of Mg, Si, or Ti because they have the lowest random and systematic errors and therefore are likely to best represent the cluster [α/Fe] (Sakari et al. 2014). Potassium is therefore another viable element for

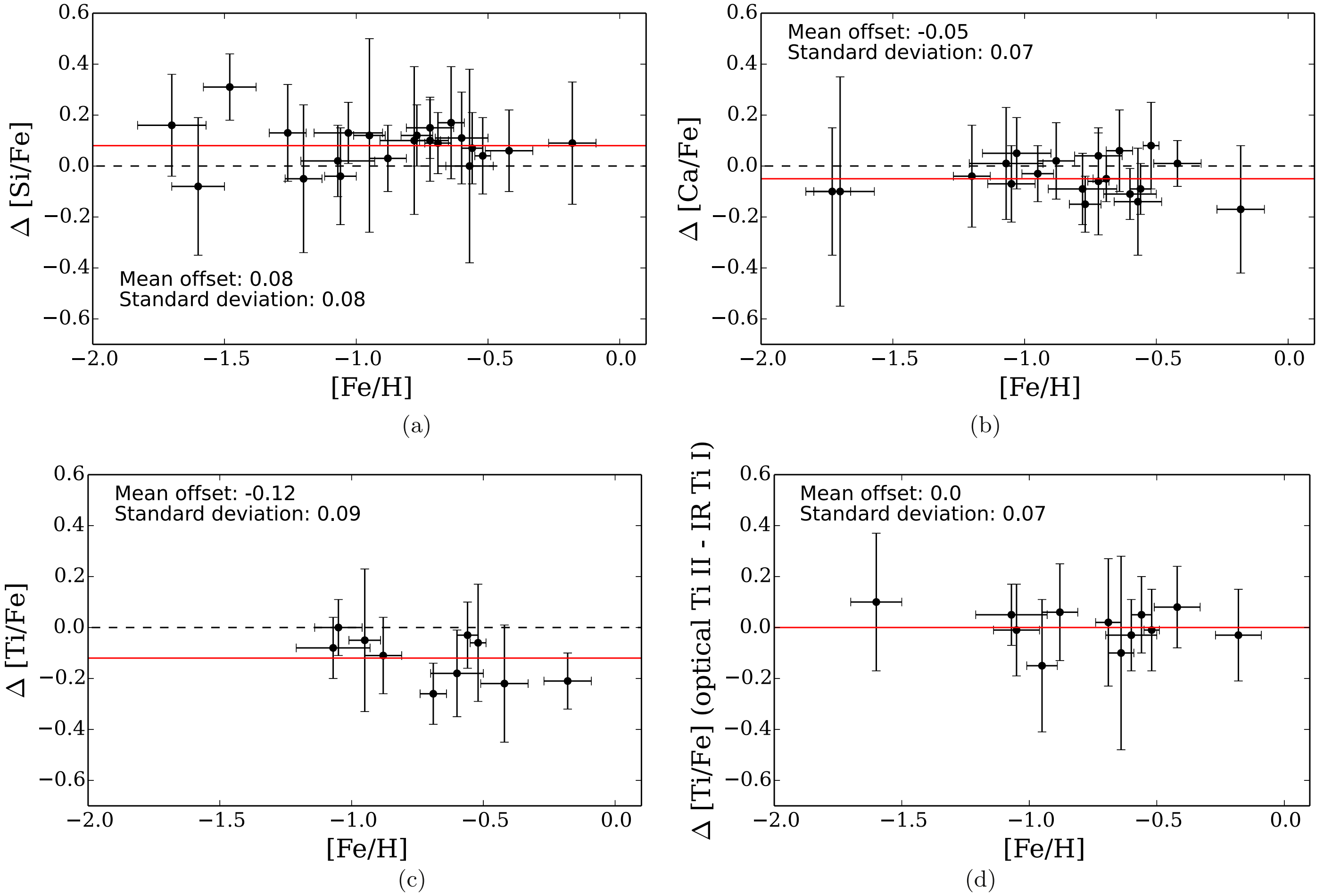

(a) (b)

(c) (d)

Figure 9. Comparisons of the *H*-band [Si/Fe] (top left), [Ca/Fe] (top right), and [Ti/Fe] (bottom) ratios with the optical values from Colucci et al. (2014) and the Appendix as a function of *H*-band [Fe/H]. The bottom left plot shows Δ[Ti I/Fe], while the bottom right plot shows the difference between optical [Ti II/Fe] and *H*-band [Ti I/Fe]. Differences are optical–*H*-band. The error bars represent 1σ random errors, the dashed lines show perfect agreement, the solid red lines show the average offsets, and the quoted values list the average offsets.

Table 4
Potassium Abundances

	[K/Fe]	*N*
B472	0.29 ± 0.20	1
B063	0.44 ± 0.10	1
B045	0.27 ± 0.10	1
B006	0.28 ± 0.10	1
B225	0.39 ± 0.07	2
B171	0.42 ± 0.15	1
B163	0.27 ± 0.08	2
B193	0.29 ± 0.10	2

abundance analyses of extragalactic targets. The spectral lines are not easy to detect in spectra of this quality, but the detections and errors would be vastly improved with higher S/N.

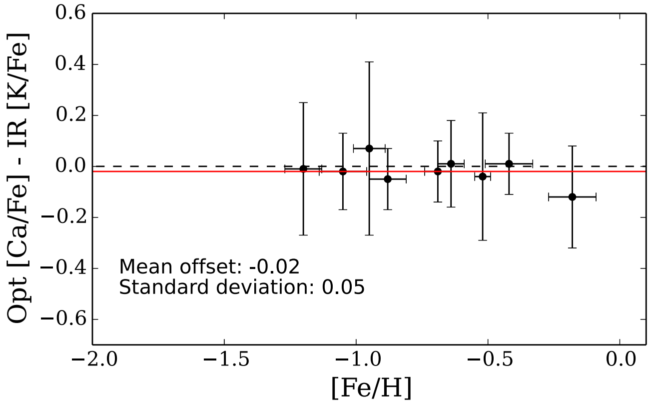

Figure 10. Comparisons of the *H*-band [K/Fe] ratios to the optical [Ca/Fe] ratios, as a function of *H*-band [Fe/H]. The error bars represent 1σ random errors, the dashed line shows perfect agreement, the solid red line shows the average offset, and the quoted value is the average offset.

5. DISCUSSION

The abundance results from Section 4 can be summarized as follows:

Iron: All clusters show good agreement between optical and *H*-band [Fe/H] ratios, most within 0.1 dex. However, this is when the optical age and metallicity from the optical are adopted (though note that the isochrone [Fe/H] is refined if the *H*-band abundance differs enough from the optical). It may be difficult to identify a viable isochrone from the *H* band alone, as discussed in Section 5.1.

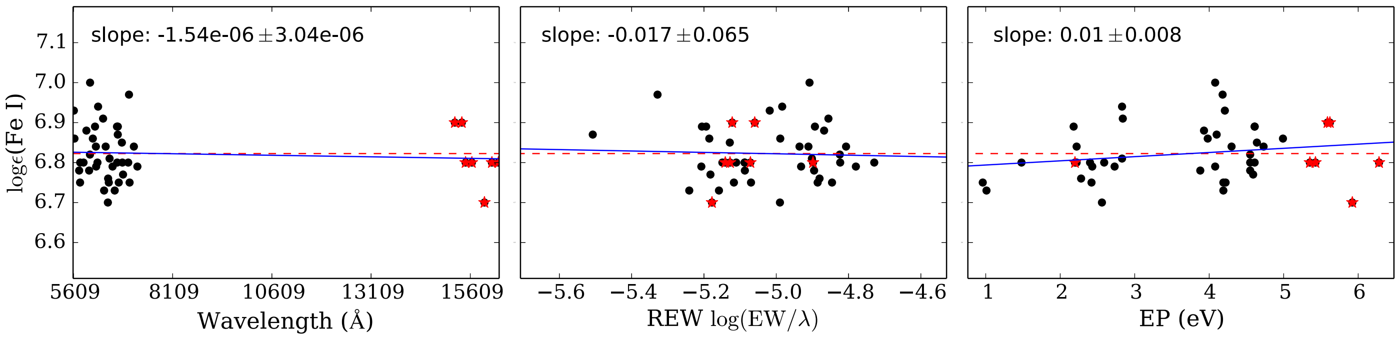

(a) Age: 12 Gyr

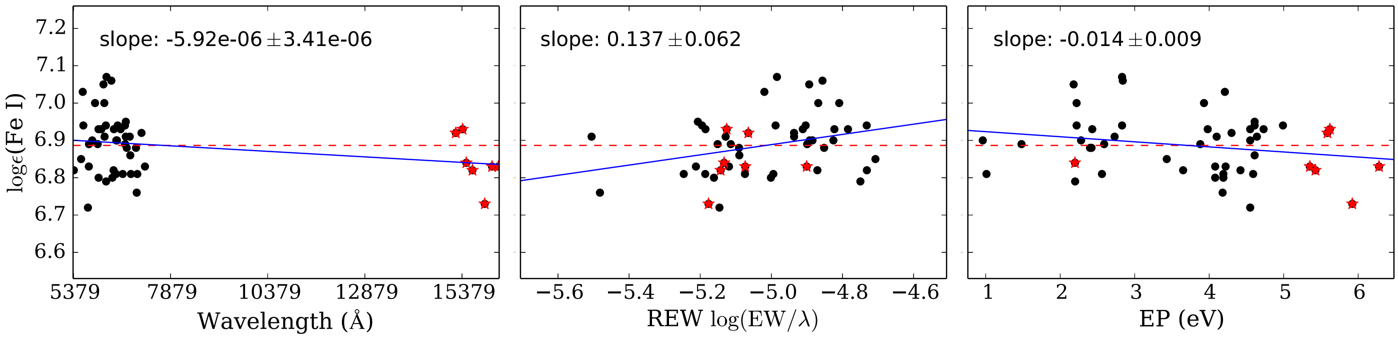

(b) Age: 5 Gyr

Figure 11. Trends in Fe I abundance with wavelength, REW, and EP, for the cluster B006. Top: abundances with the assumed optimal age of 12 Gyr. Bottom: abundances with a younger age of 5 Gyr. The optical lines (from the Appendix) are shown with black circles, while the IR lines are shown as red stars. The dashed red line shows the average Fe I abundance, while the solid blue line shows the linear least-squares fit to the points. The slopes are listed in each panel. For the 12 Gyr case, the *H*-band lines maintain the flat slopes from the optical, while adding range in wavelength and EP. The slopes from the optical points in the 5 Gyr case indicate that the age is inappropriate for B006; however, the *H*-band points do not have the parameter range necessary to constrain the cluster age.

CNO: The *H*-band [C/Fe] ratios are systematically lower than the optical Lick index values, while (with three metal-rich exceptions) the *H*-band [N/Fe] values are higher. This discrepancy is explored further in Section 5.2.

Other elements: With the exception of a few outliers in each case, the *H*-band Na, Mg, Al, Si, and Ca abundances agree well with the optical values. The *H*-band Ti abundance is in excellent agreement with the optical Ti II abundance, suggesting that the *H*-band Ti I lines are not as sensitive to NLTE effects as optical lines. The outliers could be due to issues with specific lines (as a result of, e.g., S/N or atomic data) or could reflect problems with the models of the underlying populations (though see Sections 5.1 and 5.3). The higher-precision Si and Al abundances and new O and K abundances enable the multiple populations in these M31 GCs to be probed in new ways, as discussed in Section 5.2. For elements that are not suspected to vary between stars in GCs, the general agreement between optical and the *H* band for all elements demonstrates the validity of the *H* band for abundance analyses of unresolved targets (see Section 5.4).

5.1. Determining Isochrone Parameters in the IR

High-resolution optical analyses (e.g., McWilliam & Bernstein 2008; Colucci et al. 2009, 2011, 2014; Sakari et al. 2013, 2015) utilize Fe I lines to constrain the appropriate age and metallicity of the stellar populations by minimizing trends in iron abundance with line wavelength, REW, and EP. Improperly modeled atmospheres will cause lines with different properties to have systematically offset abundances. For example, populations with too few hot stars will require larger Fe abundances to match the strengths of the highest EP lines. This technique relies on a large sample of Fe I lines with a range of wavelengths, REWs, and EPs. Even in the optical, where a large selection of Fe I lines is readily available, the line-to-line scatter prohibits better precision in cluster ages than ~1–5 Gyr (Colucci et al. 2014). Section 4.1 demonstrates that the *H* band offers only a few detectable, moderately blended Fe I lines (~2–13, depending on metallicity, S/N, and cluster velocity dispersion). The severe blending with nearby lines, especially molecular features, at this resolution renders equivalent width analyses extremely difficult. Furthermore, these Fe I lines are primarily from high-EP transitions, with most having EP > 5 eV; only two have EP < 5 eV, and those lines are not detectable in all GCs. The *H*-band Fe I lines have a variety of strengths, but only the strongest lines are detectable in the most metal-poor, high velocity dispersion GCs. This limits the usefulness of the *H* band for determining GC age without the aid of optical data. Note that while there are other, better techniques for determining GC age (e.g., isochrone fitting of partially resolved GCs, Mackey et al. 2013; or fitting age-sensitive features in the optical, Caldwell et al. 2009, 2011), this section is only concerned with whether the *H*-band spectra alone are sufficient for identifying an appropriate isochrone (and therefore for performing a detailed chemical abundance analysis).

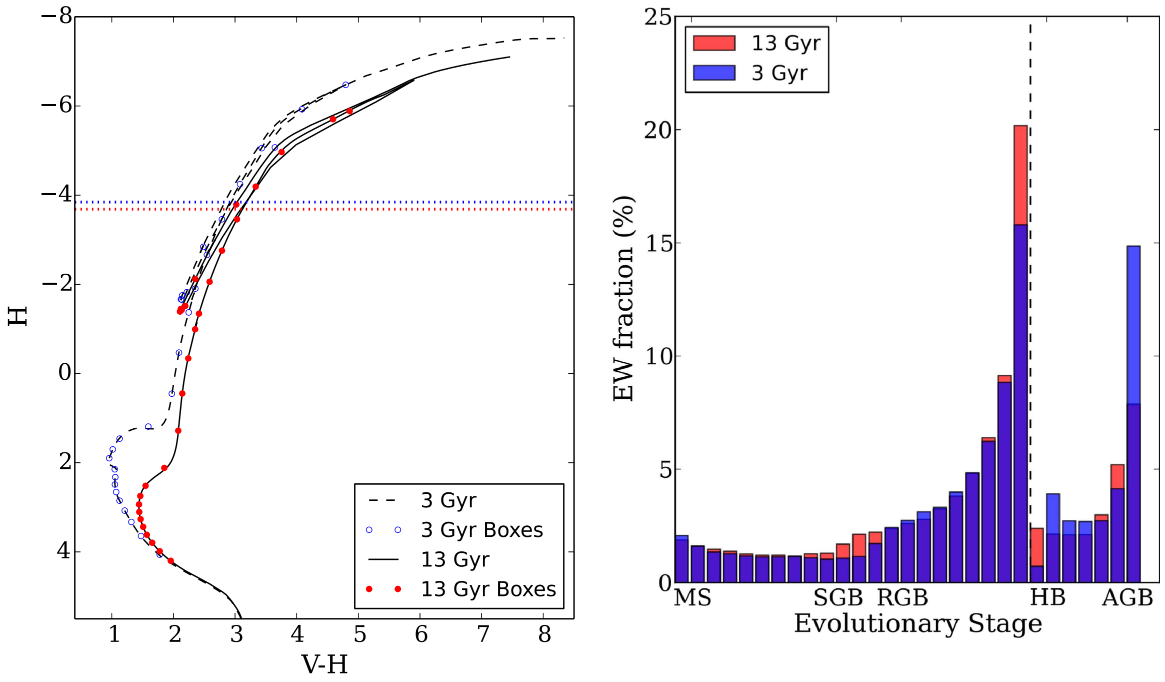

(a) (b)

Figure 12. Age effects in the *H* band. Left: BaSTI isochrones at [Fe/H] = −0.6 for ages of 13 Gyr (solid line) and 3 Gyr (dashed line). The H-R diagram boxes are shown on top of the isochrones (see Section 3.2). The half-light *H*-band levels are shown with dotted lines and are well above the HB stars. Right: the contributions to the strength of an Fe I line (at 15207 Å) from the two isochrones with different ages, per the H-R diagram box. Both examples illustrate that the *H*-band IL is dominated by the brightest RGB and AGB stars.

Table 5
Abundance Offsets When the Stellar Ages Are Lowered from 13 to 3 Gyr

		Δ[X/Fe]								
	Δ[Fe/H]	C	N	O	Na	Mg	Al	Si	Ca	Ti
MR	0.10	0.05	0.0	0.10	0.0	0.0	0.05	−0.05	0.05	0.05
MP	0.0	0.0	0.05	0.0	⋯	0.05	<0.05	0.0	<0.05	⋯

Figure 11(a) shows that for B006 ([Fe/H] = −0.69) the *H*-band Fe I lines agree well with the optical lines and add more range to the wavelength and EP plots. On their own, however, the *H*-band lines do not provide a sufficient range in REW or EP to flatten the slopes and constrain GC age. This is demonstrated in Figure 11(b), where a younger age of 5 Gyr is adopted. The optical lines indicate that 5 Gyr is not likely to be an appropriate age for B006. The *H*-band lines by themselves, on the other hand, cannot be used to rule out an age of 5 Gyr. The situation becomes even worse for clusters with low S/N or low [Fe/H], in which fewer Fe I lines are detectable. Minimizing trends in the *H*-band Fe I abundances is therefore not a viable way to constrain the cluster age.

However, even with the younger age of 5 Gyr, the *H*-band abundances still converge on roughly the same metallicity ([Fe/H] = −0.66), suggesting that the *H* band is less sensitive to cluster age than the optical (at least for GCs older than ~3 Gyr). This can be understood simply by considering the relative contributions from various subpopulations in the *H* band. Figure 12(a) shows sample isochrones for a GC with [Fe/H] = −0.6 at ages of 13 Gyr and 3 Gyr. Figure 12(b) then shows the fractional contribution from each box to the strength of an Fe I line (at 15207 Å). These two figures illustrate that the *H*-band continuum level and Fe I line strength are dominated by the tip of the RGB and AGB stars. The turnoff stars have very little effect on the Fe I line, suggesting that cluster age will be

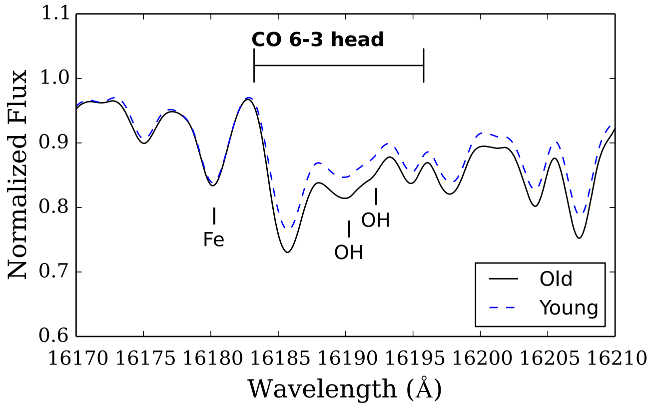

Figure 13. Syntheses of a CO band head in a GC with [Fe/H] = −0.5, utilizing two different isochrones: an old 13 Gyr one (the solid black line) and a younger 3 Gyr one (the dashed blue line). The younger isochrone requires a larger C abundance to reproduce the strength of this feature, but a corresponding increase in [Fe/H] means that the relative [C/Fe] ratio changes by only 0.05 dex.

Table 6
Integrated Abundances When [C/Fe], [N/Fe] and ^{12}C/^{13}C Variations along the RGB Are Adopted

	[Fe/H] = −0.5	[Fe/H] = −1.7
Δ[C/Fe]	−0.50	−0.50[a]
Δ[N/Fe]	1.0	0.95
^{12}C/^{13}C	5–6	⋯

Note.
[a] Note that some of the CO features are undetectable in the spectra of the most metal-poor clusters.

less important for determining [Fe/H] in the *H* band (though note, however, that the RGB is slightly offset in the 3 Gyr case, and that the younger isochrone's AGB has a greater effect on the Fe I line).

To test the effects of GC age on the abundances of the other elements, *H*-band abundances were determined for synthetic metal-rich ([Fe/H] = −0.5) and metal-poor ([Fe/H] = −1.7) clusters, each with ages of 13 and 3 Gyr. The total abundance differences for the two clusters are provided in Table 5. The differences in relative [X/Fe] ratios are all $\lesssim$0.1 dex. Figure 13 then shows syntheses of a CO band head in B171 (starting at 16183 Å), where the [C/Fe] from the old population is adopted. Lowering the age has slightly weakened the CO features; bringing the line strengths into agreement requires increasing [C/H] by 0.15 dex for the younger isochrone. A similar increase in [Fe/H] (by 0.1 dex) means that Δ[C/Fe] = 0.05 for the 3 Gyr case. The effect of having a younger age by 10 Gyr is therefore not significant for the abundances determined in this analysis, at least for clusters older than ~3 Gyr.[21]

To summarize, *H*-band IL spectra do not have enough Fe I lines to constrain GC age in the same way as the optical. However, for GCs older than ~3 Gyr, the precise age has a much smaller impact on *H*-band abundances than on optical abundances. As long as an appropriate isochrone metallicity is selected, an age that is off by as much as 10 Gyr will only lead to negligible abundance offsets in old GCs.

5.2. Signatures of Multiple Populations

All bona fide, classical MW GCs are known to host significant star-to-star abundance variations. All GCs have stars that exhibit a Na/O anticorrelation, while some massive, metal-poor GCs also show Mg/Al anticorrelations (e.g., Carretta et al. 2009b). Some GCs have significant CN variations (such as 47 Tuc; Briley et al. 2004). A few of the most massive GCs host spreads in heavy neutron-capture elements such as Ba and Eu (e.g., M15; Sneden et al. 1997), while an even smaller number host Fe variations (e.g., Carretta et al. 2010b). As Colucci et al. (2014) have pointed out, interpreting the integrated abundances of GCs in terms of abundance variations within the clusters is nontrivial. The correlations are observed between individual stars in a given cluster, while IL abundances represent a flux-weighted average from a single cluster. However, deviations from the "primordial" abundances are inferred to exist in distant, partially resolved M31 GCs based on, for example, enhanced integrated [Na/Fe], deficient integrated [Mg/Fe], or abundance correlations with cluster mass (Schiavon et al. 2013; Colucci et al. 2014; Sakari et al. 2015).

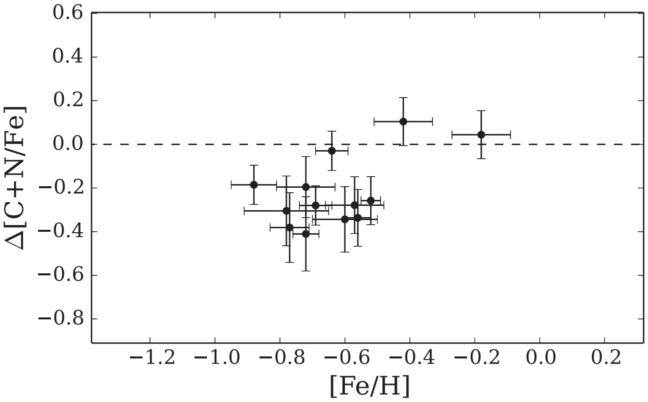

Figure 14. Δ[(C + N)/Fe] (optical–*H*-band) as a function of *H*-band [Fe/H]. The dashed line shows perfect agreement.

These *H*-band abundances offer the chance to study new elements, like O, and to probe lines in a wavelength regime that is dominated by different stars than in the optical. This section explores what can be learned about multiple populations in distant GCs from a combination of optical and *H*-band IL spectroscopy, focusing on CN variations (Section 5.2.1), the Na/O anticorrelation (Section 5.2.2), the Mg/Al anticorrelation (Section 5.2.3), and Fe spreads (Section 5.2.4).

5.2.1. CN

This section examines the possibility that the disagreements between the *H*-band and optical Lick index CN abundances could be due to the presence of strong star-to-star CN variations within the GC. In particular, the different wavelength regimes may be sensitive to different stellar subpopulations because the *H* band is only sensitive to the tip of the RGB stars while the optical is more sensitive to hot stars.

Variations along the RGB. In addition to the variations that occur between the multiple GC populations, surface C and N abundances (and ^{12}C/^{13}C ratios) also vary as a star evolves up the RGB (see, e.g., Gratton et al. 2000). The IR is predominantly sensitive to the evolved tip of the RGB stars, while the bluer, optical Lick indices may be more sensitive to the less-evolved RGB stars that have "normal" (i.e., pre-dredge-up) C and N abundances.

To test this, synthetic clusters were created with [C/Fe], [N/Fe], and ^{12}C/^{13}C variations along the upper RGB, one metal-rich ([Fe/H] = −0.5) and the other metal-poor ([Fe/H] = −1.7). The variations from Gratton et al. (2000) are adopted: initial values of [C/Fe] = 0, [N/Fe] = 0, and ^{12}C/^{13}C = 40 are adopted for all lower RGB stars; above the RGB bump the ^{12}C/^{13}C is a step function down to 5, while [C/Fe] and [N/Fe] linearly change along the RGB to final values of −0.5 and 1.0, respectively. All of the evolved HB and AGB stars are assumed to have the same values as the tip of the RGB stars. Note that these values are for more *metal-poor* field stars: metal-rich stars are expected to show smaller variations. However, this exercise provides a good test of the most extreme changes that could occur. These composite synthetic spectra are then treated as the observed spectra, and best-fitting integrated abundances are determined from the composite

---

[21] Although it is not shown here, the effects of adopting a blue HB are similarly negligible.

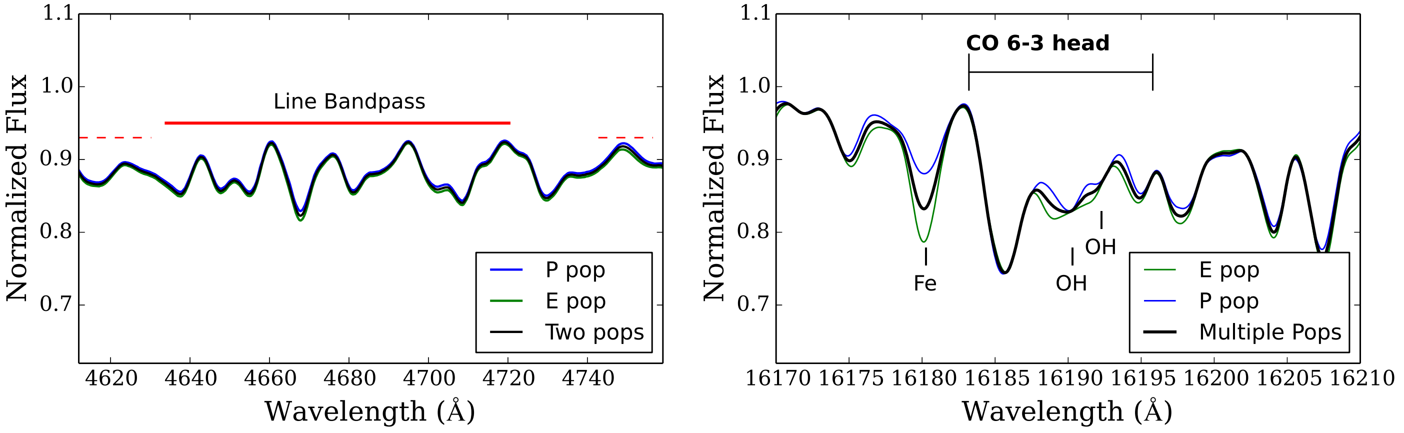

(a)

Figure 15. Syntheses of C-sensitive features in a metal-rich cluster ([Fe/H] = −0.5) with multiple populations. Left: the 4668 Å feature at a Lick index resolution of 5 Å. Right: the 16183 Å band head with B171's line broadening. The blue lines show syntheses with abundances typical of a GC's "primordial" population, while the green lines show syntheses with the abundances typical of the "extreme" population (enhanced N, lower C). The black line shows syntheses with a population composed of 60% extreme and 40% primordial.

spectrum. The derived [C/Fe], [N/Fe], and $^{12}C/^{13}C$ ratios are shown in Table 6 and match the abundances that were input for the tip of the RGB, HB, and AGB stars. This demonstrates that the H-band integrated [C/Fe], [N/Fe], and $^{12}C/^{13}C$ ratios are largely insensitive to the variations going up the RGB and reflect the abundances of the most-evolved RGB stars.

If the optical IL features are more sensitive to the less-evolved stars, they should have higher [C/Fe] and lower [N/Fe] ratios, but the total amount of [(C + N)/Fe] should remain the same, since the abundance changes occur as C is converted into N. Note that this comparison assumes that the optical C and N are sensitive to the same stellar populations, which may not be true given the wavelength separation between the C_2 and CN indices. Figure 14 compares the [(C + N)/Fe] ratios, which are not equal between the optical and IR. This suggests that the offsets cannot *only* be due to the optical Lick ratios probing stars farther down the main sequence. Other systematic possibilities are that the Lick C and N abundances are not tracing the same populations or that there are other unknown systematic offsets between the optical and H band.

Varying sensitivities to multiple populations between the H band and optical. Another possibility is that the optical and H band have different sensitivities to the multiple populations within the GCs. C, N, and O variations are observed between stars in Galactic GCs. For instance, 47 Tuc exhibits a strong bimodality in CN-weak and CN-strong stars that persists through the main sequence (e.g., Briley et al. 2004), and all MW GCs show variations in O (typically seen as a Na/O anticorrelation; e.g., Carretta et al. 2009b). As with the variations going up the RGB, the effects of multiple CN populations can be examined by creating a synthetic population with multiple populations and deriving a single IL abundance. The clusters are assumed to have C, N, O, and Na variations. None of these elements are expected to significantly change the temperature of the RGB (VandenBerg et al. 2012), so the same isochrones are used for each population. Note that variations along the RGB were not included within each subpopulation.

Figure 15(b) shows the syntheses of GCs with multiple populations. In both the optical and the H band, the IL values fall in between the range from the "primordial" and "extreme" populations. The best-fitting values from the optical and H band are identical, suggesting that the optical versus H-band offset is likely not due to varying sensitivity to GC multiple populations.

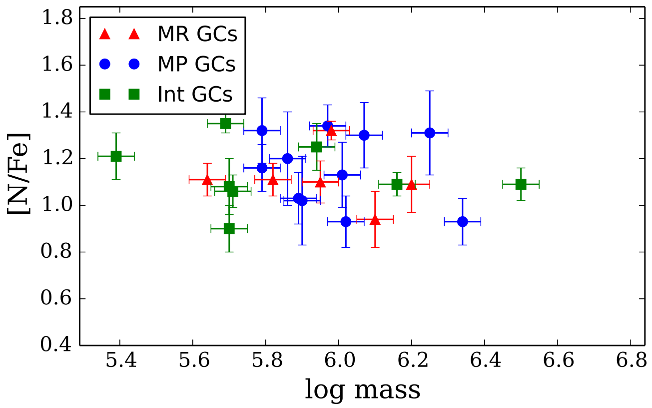

Figure 16. [N/Fe] vs. cluster mass. The points are grouped according to GC metallicity. The metal-poor (MP) GCs have [Fe/H] < −1.2, the metal-rich (MR) ones have [Fe/H] > −0.8, and the intermediate-metallicity (Int) ones fall in between. There is no convincing trend with mass in any of the subgroups, though the mass range is not very large.

Trends with cluster mass. In their Lick index analysis of MW GCs, Schiavon et al. (2013) detected a metallicity-dependent trend of increasing [N/Fe] with increasing cluster mass. They interpreted this as a signature of multiple populations, where massive GCs are able to form a larger fraction of "second-generation" stars. Trends with mass are also investigated with the H-band abundances. Figure 16 shows [N/Fe] versus cluster mass, utilizing the cluster masses from Schiavon et al. (2013). The clusters are grouped by metallicity, as in Schiavon et al. No convincing trend is seen in any of the metallicity groups. This is unsurprising given that the H band is dominated by the tip of the RGB stars: all the tip of the RGB stars have enhanced [N/Fe] because of normal stellar evolutionary processes, and the H-band [N/Fe] ratios therefore should not depend on cluster mass. Note, however, that the

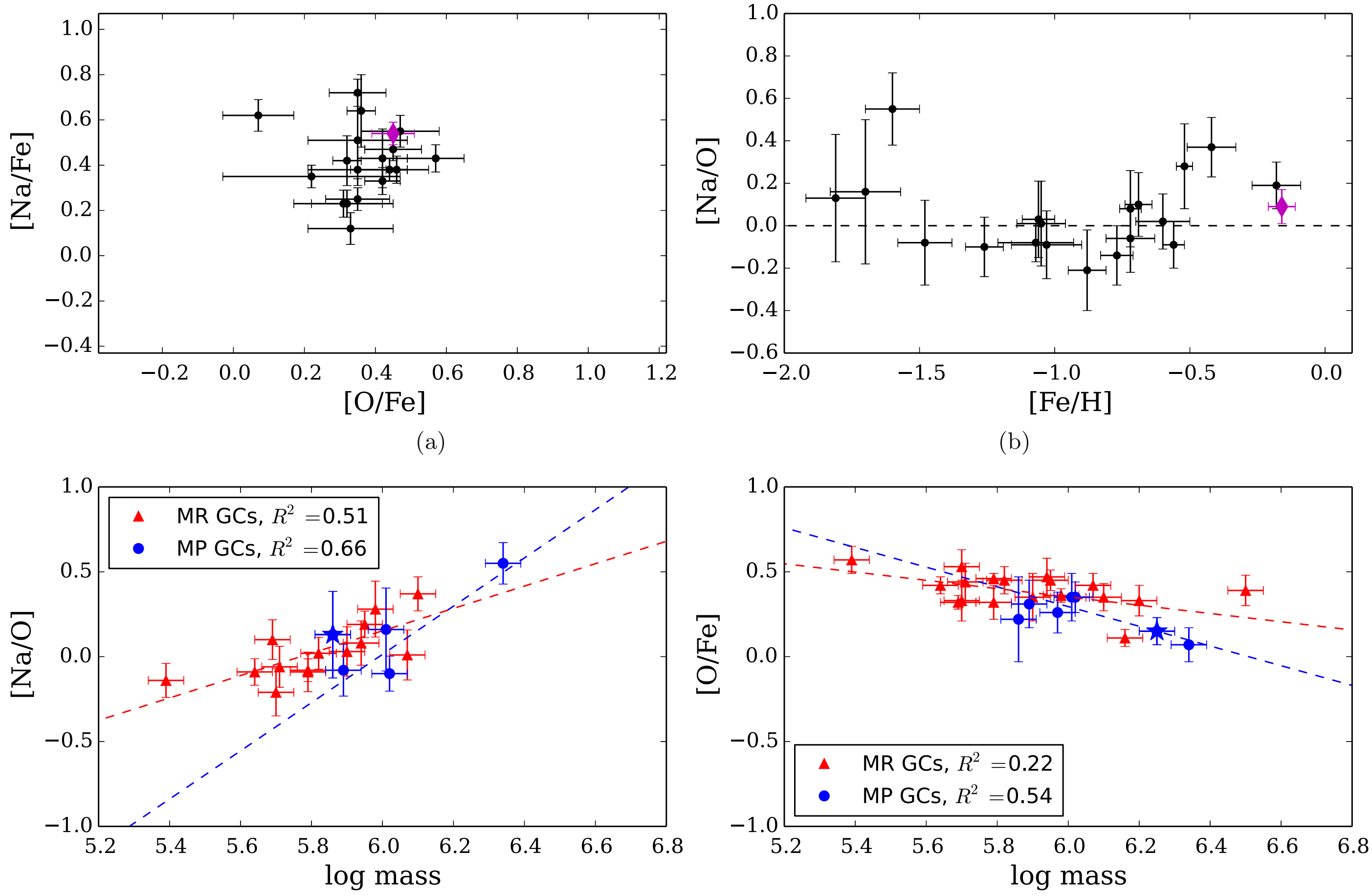

(a) (b)

(c) (d)

Figure 17. Top left: optical [Na/Fe] vs. *H*-band [O/Fe]. The magenta diamond shows B193, whose *H*-band [Na/Fe] is utilized in lieu of an optical abundance. Top right: [Na/O] (with optical Na and *H*-band O) vs. cluster [Fe/H]. The dashed line shows equal [Na/Fe] and [O/Fe]. Bottom left: [Na/O] vs. cluster mass (from Schiavon et al. 2013). The clusters are grouped by metallicity: metal-poor (MP) GCs have $[Fe/H] < -1.2$. The dashed lines show fits to each metallicity group, with coefficients of determination shown. Bottom right: [O/Fe] vs. cluster mass.

mass range of these GCs is not as large as the Schiavon et al. sample, and these results may change if more GCs are included.

5.2.2. Na/O

The Na/O anticorrelation is well established within MW GCs (Carretta et al. 2009b). Extragalactic GCs have been inferred to host Na/O anticorrelations since many have high integrated [Na/Fe] (Colucci et al. 2014; Sakari et al. 2015). Figure 17(a) shows the optical [Na/Fe] versus *H*-band [O/Fe] (except for B193, whose *H*-band [Na/Fe] is used in lieu of an optical value). There is no clear anticorrelation; however, in IL an anticorrelation would not be expected. All of the clusters lie within the range of individual MW GC stars (see Carretta et al. 2009b) in the region represented by the "intermediate" populations (see the descriptions in Carretta et al. 2009a). Only one GC, B012, falls in the region of the "extreme" population.

Trends with metallicity and mass. Figures 17(b) and (c) show the *H*-band IL [Na/O] ratios versus [Fe/H] and cluster mass (from Schiavon et al. 2013). Note that not all of the GCs have [Na/Fe] abundances, particularly two of the most massive GCs, B088 and B225. There have been some hints that the extent of the Na/O anticorrelation may change with metallicity (e.g., Figure 5 in Carretta et al. 2009b); however, Carretta et al. (2010a) argue that [Fe/H] most strongly correlates with the fraction of "extreme" stars (i.e., those that are the most enhanced in Na and deficient in O). The extent of the Na/O anticorrelation is also expected to vary with cluster mass because the relative numbers of stars in various populations may depend on mass (e.g., Carretta et al. 2009a, 2010a; Schiavon et al. 2013). Figure 17(b) shows no obvious trend with metallicity, though Figure 17(c) hints at a possible trend with GC mass. Again, the clusters are grouped by metallicity; the metal-rich GCs appear to have the strongest correlation of [Na/O] with mass. This abundance trend follows the trend found by Colucci et al. (2014), which showed an increasing integrated [Na/Fe] with absolute magnitude and velocity dispersion (as expected since their Na abundances were utilized for this comparison). Figure 17(d) then examines the trend in integrated [O/Fe]. The trend is weak for the metal-rich clusters but may be stronger for the handful of metal-poor clusters.

5.2.3. Mg/Al

Mg/Al anticorrelations have been observed in the optical within the most massive, metal-poor ($[Fe/H] \lesssim -1.2$) Galactic

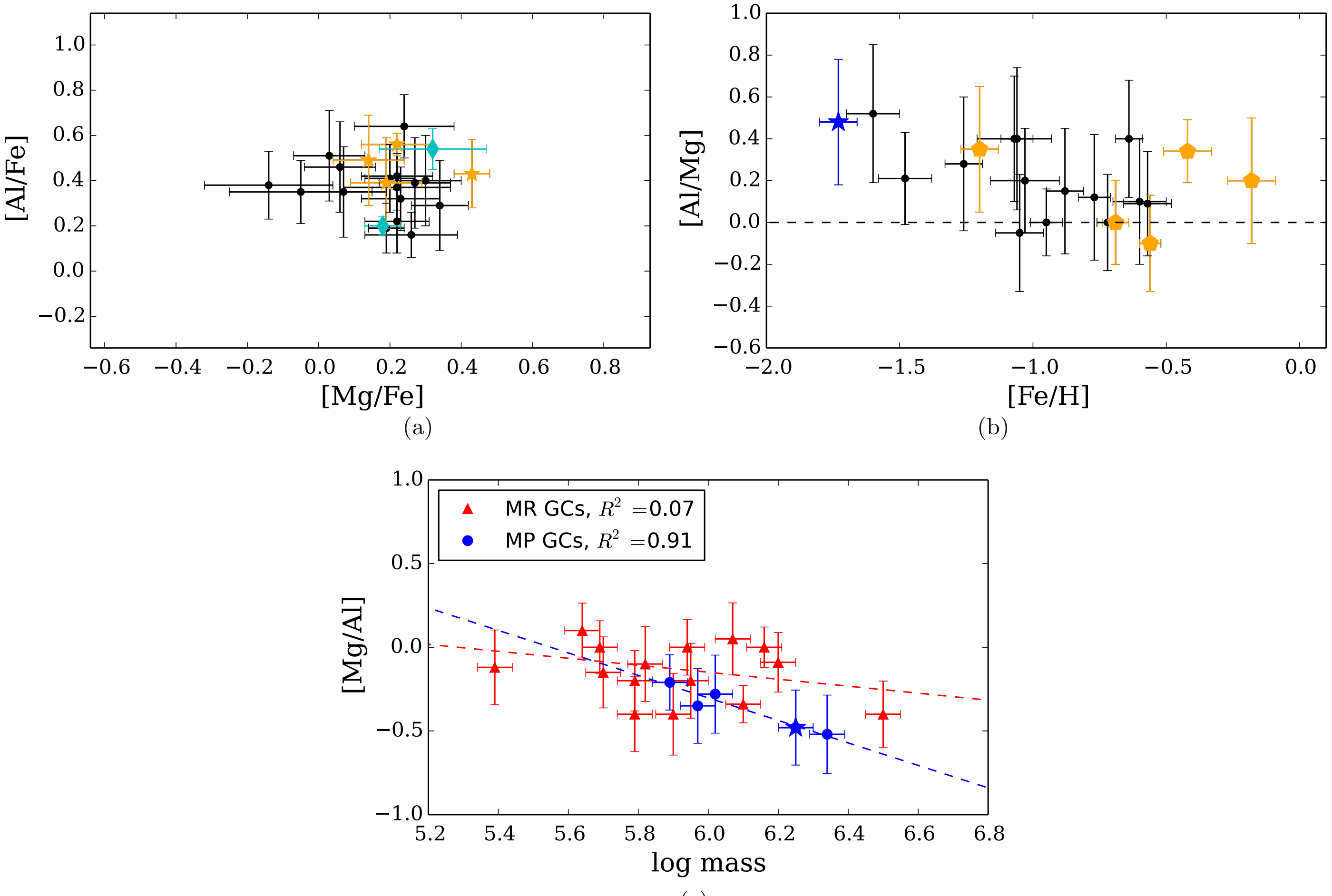

(a)

(b)

(c)

Figure 18. Top left: *H*-band [Al/Fe] vs. [Mg/Fe]. The cyan diamonds show B171 and B403, whose optical [Al/Fe] abundances are utilized in lieu of *H*-band values. Again, the orange pentagons show clusters whose [Al/Fe] ratios are determined from strong lines. Top right: [Al/Mg] vs. cluster *H*-band [Fe/H]. The dashed line shows perfect agreement. Bottom: [Al/Mg] vs. cluster mass. Metallicity bins and fits are as in Figure 17(c). In panels (b) and (c), B088 is shown with a blue star.

GCs (e.g., Carretta et al. 2009b) and in the IR for several additional clusters (Meszaros et al. 2015). Figure 18(a) shows *H*-band [Al/Fe] versus [Mg/Fe]; the orange pentagons show the GCs whose [Al/Fe] ratios were determined from strong lines ($-4.7 < \mathrm{REW} < -4.5$), while the cyan diamonds show clusters whose optical [Al/Fe] ratios are used (since they do not have *H*-band Al abundances). There is no clear anticorrelation in the IL ratios.

Trends with metallicity and mass. Figure 18(b) then compares [Mg/Al] versus *H*-band [Fe/H]. No trends are seen in any of the subgroups, though if optical [Mg/Fe] ratios are used, B088 creates a slight trend at the metal-poor end. The [Mg/Al] ratio is then plotted against cluster mass in Figure 18(c), again grouped into metallicity bins (since the presence of the Mg/Al anticorrelation may be metallicity-dependent; Carretta et al. 2009b). Note that Colucci et al. (2014) found a positive trend in [Mg/Fe] and [Al/Fe] with mass in metal-rich GCs, but a negative trend in massive metal-poor GCs. With *H*-band Al and Mg, no significant trends in [Mg/Al] are seen in the metal-rich population. Although there is a correlation in the metal-poor population, this is due to only five GCs, one of which is B088, whose optical and *H*-band Mg abundances are very discrepant. More metal-poor clusters are needed to assess whether or not such a trend with mass exists.

The case of B088. Recall that B088's [Mg/Fe] shows significant disagreement between the optical and the *H* band. Colucci et al. (2014) find a very low optical $[\mathrm{Mg/Fe}] = -0.48 \pm 0.02$, while the *H*-band value from this paper is higher by 4σ. B088 is a massive ($\log M = 6.25$; Schiavon et al. 2013), metal-poor ($[\mathrm{Fe/H}] = -1.71$) GC and may therefore host a significant Mg/Al anticorrelation. For instance, the more metal-poor, similarly massive MW GC M15 has known Mg/Al variations and a low optical IL [Mg/Fe] (Sakari et al. 2013). One way to create an offset in abundance between the optical and the *H* band might be to introduce a temperature spread on the RGB and examine spectral lines with varying sensitivities to the two populations. One way to create a temperature split on the RGB is varying [Mg/Fe] (VandenBerg et al. 2012).

To test if Mg variations can explain the disagreement between the optical and the IR, two synthetic populations were created. The "primordial" (P) population has $[\mathrm{O/Fe}] = [\mathrm{Mg/Fe}] = +0.4$, while the "extreme" (E) population has $[\mathrm{O/Fe}] = -0.2$ and $[\mathrm{Mg/Fe}] = -0.6$. The cluster is assumed to have 50% of each population. This assumption is unrealistic given the small numbers of "extreme" stars found in most GCs, but again, this should test the maximal offsets that could occur. Isochrones with α-element enhancement are utilized for the P population, while solar-scaled ones are selected for

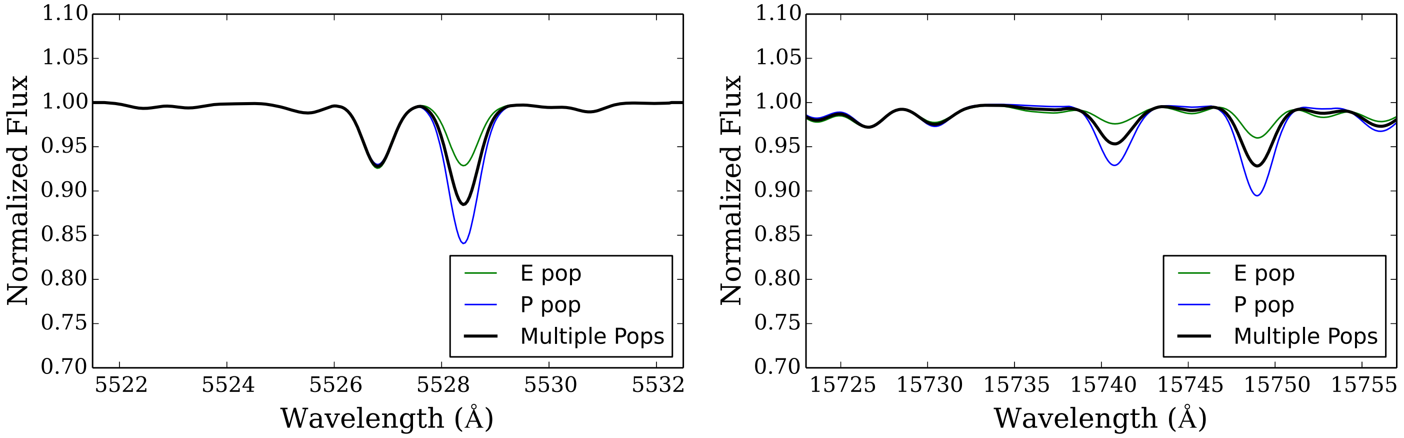

Figure 19. Syntheses of Mg I lines in a B088-like cluster, with [Fe/H] = −1.84. Left: the optical 5528 Å line. Right: the infrared 15740 and 15748 Å spectral lines. The blue lines show syntheses with abundances typical of a GC's "primordial" population, while the green lines show syntheses with the abundances typical of the "extreme" population. The black line shows syntheses with a population composed of 50% of each.

the E population. Figure 19 shows that the synthesis with hypothetical multiple populations falls in between those for the E and P populations alone. Most importantly, when the synthetic, multiple-population spectra are analyzed as single spectra, the *H* band and the optical converge on the same value for the two lines, [Mg/Fe] = −0.01. This indicates that the disagreement between the optical and the *H* band is likely *not* due to different sensitivities to the multiple populations if the only variations are in O, Na, Mg, and Al.

5.2.4. Possible Fe Spreads?

Another way to introduce temperature shifts on the RGB is by invoking a metallicity spread within the cluster. Indeed, B088's *Hubble Space Telescope* (*HST*) color–magnitude diagram (Perina et al. 2009) hints at the possibility of a metallicity spread on the RGB, while its high ellipticity ($\epsilon = 0.28$; Barmby et al. 2007) suggests that it is not a typical GC. Again, synthetic populations were created to test this effect, one with [Fe/H] = −1.31 and the other with [Fe/H] = −2.14; the two subpopulations were assumed to have equal numbers of stars. Treating the synthetic composite spectrum as an observed spectrum, the *H*-band lines that were detectable in B088 (all from high-EP transitions) converge on an integrated [Fe/H] = −1.55. Utilizing the optical EWs from Colucci et al. (2014), the optical values converge on an average [Fe/H] = −1.6. Even with an [Fe/H] spread introduced, the average IL [Fe/H] ratios are approximately the same between the optical and the *H* band and fall between the two "real" values, in agreement with the values derived for B088. However, there is an important caveat here: the introduction of a metallicity spread has changed the slopes with REW and (to a lesser extent) EP in the optical, and this may affect the derived GC age.

Without altering the GC age, however, introducing an Fe spread could lead to an offset in Mg I between the optical and the IR. Comparisons between the 5528 Å and IR 15740, 15748, and 15764 Å lines suggest that an offset of Δ[Mg/Fe] $\sim$ 0.2 dex can be created just from invoking a metallicity spread. Thus, offsets between the optical and IR *may* probe the existence of Fe spreads within GCs, provided that temperature-sensitive lines are utilized. More detailed tests of this phenomenon are needed to verify if this is an accurate test of Fe spreads within GCs.

5.3. The AGB/RGB Ratio

Though the *H*-band light is dominated by the tip of the RGB stars, AGB stars are also a major contributor to the IL. Among other things, the models of the underlying stellar populations that are utilized in this paper rely on (1) the assumption of an IMF to populate the isochrones and (2) prescriptions for how the AGB is modeled and how long stars will remain on the AGB. Recently, APOGEE *H*-band abundances of Galactic GC giant stars combined with ground-based photometry suggest that the ratio of AGB to RGB stars may be higher in the *H* band than previously determined from the optical (García-Hernández et al. 2015, S. Meszaros et al. 2016, in preparation; however, possible selection effects are very difficult to evaluate). AGB stars are likely to have a strong effect on an *H*-band IL spectrum and may be a source of systematic errors in the integrated abundances. To test the effect of a high AGB/RGB ratio in the *H* band, the number of AGB stars was manually increased in a GC with [Fe/H] = −0.5, and the effects on the derived abundances were determined. In general, when the number of AGB stars increases, the IL spectral lines become stronger; this means that lower abundances are needed to fit the observed spectra. However, for reasonable AGB/RGB ratios, these offsets are $\lesssim$0.05 dex. Significant abundance differences ($\sim$0.1 dex) are not evident until the AGB/RGB ratio becomes fairly high ($\sim$50%); even then, the offsets in differential [X/Fe] ratios are lower than 0.1 dex. It therefore seems that the AGB/RGB ratio is not likely to significantly affect the derived IL abundances.

Stochastic sampling of the AGB and RGB may have a larger effect on the *H*-band abundances, even in these massive clusters; this will be explored in a future paper.

5.4. The Chemical Evolution of M31's GCs

In most GCs, Si, Ca, Ti, and Fe are not expected to vary between stars within the GC, and their integrated abundances should reflect the abundances of a GC's birth environment. *H*-band Si, Ca, Ti, and Fe can therefore be used for chemical tagging and chemical evolution studies, as in the optical (e.g.,

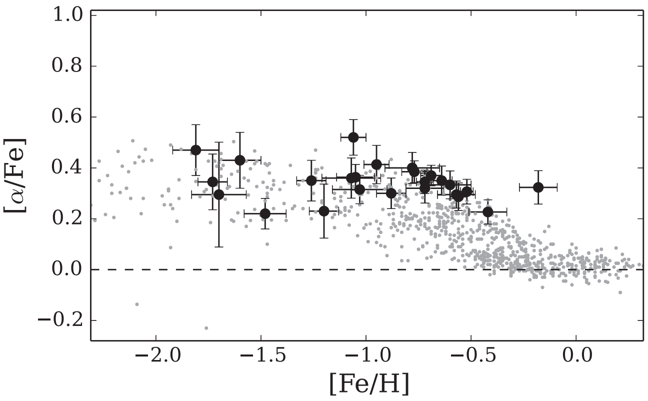

Figure 20. $[\alpha/\text{Fe}]$ vs. [Fe/H] in the M31 GCs (black circles) and MW field stars (gray points; from the sources in Venn et al. 2004, with supplements from Reddy et al. 2006).

Colucci et al. 2012, 2013, 2014; Sakari et al. 2015). Figure 20 shows *H*-band integrated $[\alpha/\text{Fe}]$ versus [Fe/H] for the M31 GCs, where α is an average of Si, Ca, and Ti (or one or two of the elements if all three are not available). Also shown are MW field stars from Venn et al. (2004) and Reddy et al. (2006). M31 field stars are not shown because the field stars are too faint for high-quality analyses; however, the M31 field stars are expected to follow the MW field stars, especially in this metallicity range. As expected from optical analyses, the M31 GCs do generally track the MW field stars. As in the optical, B193's $[\alpha/\text{Fe}]$ is slightly higher than MW field stars at the same $[\text{Fe/H}] \sim -0.2$ (see Colucci et al. 2014); this indicates that B193 may have formed in an environment that experienced rapid chemical enrichment.

However, high-precision Ca and Ti abundances can be obtained from the optical along with abundances of a wider variety of elements. Is the optical therefore the preferred wavelength regime for IL analyses, or does the *H* band offer any significant advantages over the optical? Section 5.1 demonstrated that *H*-band abundances are less sensitive to GC age (and HB morphology) than the optical. In situations when GC age is poorly constrained, systematic uncertainties may be lower in the *H* band. Furthermore, GCs that are heavily obscured and reddened by dust will be much easier to observe in the IR than in the optical.

It is also worth noting that there are additional spectral lines in the *J* and *K* bands. Expanded IR IL spectroscopy with more wavelength coverage would increase the number of observed elements and the precision in a single abundance.

6. CONCLUSIONS

This paper has presented an *H*-band IL spectroscopic analysis of 25 bright GCs that are associated with M31. The target GCs span a wide range in metallicity (from $[\text{Fe/H}] = -1.8$ to -0.2), a moderate range in total mass (from $\log \text{mass} \sim 5.4$ to ~ 6.5), and a small range in age (from ~ 6.5 to 14 Gyr). All the GCs were previously targeted for high-resolution optical spectroscopy, enabling a comparison between *H*-band and optical abundances. The primary results from this study are as follows:

1. The *H* band offers a wide variety of spectral lines that complement the optical. In addition to the handful of additional Fe I lines, the *H* band offers intermediate and strong Mg I, Al I, and Si I lines and weaker Na, Ca, Ti, and K lines. Molecular CO, CN, and OH features allow determinations of C, N, and O abundances. $^{12}\text{C}/^{13}\text{C}$ ratios cannot be well constrained in these spectra, but could be measurable in higher quality spectra from metal-rich targets.
2. The Fe I lines in the *H* band provide Fe abundances that are in excellent agreement with the optical abundances. Although there is a small offset (~ 0.05) between the optical and *H*-band [Fe I/H] ratios, this may reflect different NLTE corrections between the optical and IR (e.g., García-Hernández et al. 2015). Despite the small offset, the *H*-band lines agree with the optical trends in Fe abundance with line wavelength, REW, and EP. However, the parameter ranges are smaller among the *H*-band lines, and it may not be possible to constrain the GC age without complementary optical data (photometric or spectroscopic). However, the *H*-band abundance ratios are relatively insensitive to GC age, at least for GCs older than ~ 3 Gyr.
3. The *H*-band [C/Fe] and [N/Fe] abundances reflect typical tip of the RGB stellar abundances. However, they are systematically offset from the C and N abundances derived from the optical 4668 Å Lick index.
4. With a few exceptions, the abundances of Na, Mg, Al, Si, and Ca are in excellent agreement between the optical and the *H* band. The *H*-band Ti I abundances agree well with the optical Ti II abundances, suggesting that the *H*-band lines may be less sensitive to NLTE effects than the optical ones.
5. The *H* band offers new [O/Fe] and [K/Fe] abundances that are not available in the optical. The K abundances trace Ca, as predicted from stars in the MW.
6. With the detailed *H*-band abundances, multiple populations in extragalactic GCs can be explored in new detail. The integrated [Na/O] ratio is found to roughly correlate with cluster mass, suggesting that the relative numbers of "second-generation" stars may increase with cluster mass. No convincing similar trend was found for [Mg/Al].
7. As expected for GCs associated with a massive spiral galaxy, the *H*-band $[\alpha/\text{Fe}]$ ratios track MW field stars, demonstrating that *H*-band IL spectroscopy can be utilized for chemical tagging analyses of unresolved targets.

Thus, *H*-band IL spectroscopy will be a valuable tool for studying more distant, unresolved stellar populations, particularly those that are highly reddened.

The authors thank the anonymous referee for suggestions that improved the manuscript. The authors also thank Chris Sneden for developing the *synpop* version of `MOOG` and maintaining the code, Andrew McWilliam for discussions regarding integrated light analyses, and Masen Lamb for discussions regarding IR syntheses. CMS acknowledges funding from the Kenilworth Foundation. DB acknowledges support from grant RSF 14-50-00043. CAP is thankful to the Spanish MINECO for funding through grant AYA2014-56359-P. TCB acknowledges partial support for this work from grants PHY08-22648, Physics Frontier Center/Joint Institute or Nuclear Astrophysics (JINA); and PHY 14-30152, Physics Frontier Center/JINA Center for the Evolution of the Elements (JINA-CEE), awarded by the US National Science Foundation.

Table 7
Observation Information and Derived Isochrones for New Optical Data

	Observation Dates	$t_{\rm exp}$ (s)	S/N[a] (6000 Å)	$v_{\rm helio}$ (km s^{-1})	σ (km s^{-1})	Isochrone [Fe/H]	Age (Gyr)
B006	2009 Oct 11, 14, 18, 19, 20	10565	140	−236.3 ± 0.5	10.56 ± 0.4	−0.70	12
B063	2009 Nov 15, 25, Dec 12, 13, 16	11997	200	−304.2 ± 0.5	15.15 ± 0.6	−1.01	14
B171	2009 Dec 17, 18, 20, 21 2010 Jan 10, 18	16200	250	−267.7 ± 0.5	16.81 ± 0.5	−0.69	13
B311	2009 Oct 24, 27, Nov 12, 17	11016	160	−515.6 ± 1.0	12.70 ± 0.4	−1.62	13
B472	2009 Dec 23, 2010, Jan 4, 5, 13	10800	120	−120.9 ± 0.5	14.37 ± 0.6	−1.01	11

Note.
[a] S/N is per resolution element; there are 2.7 pixels per resolution element.

Table 8
Line List for Optical Abundances

				EW (mÅ)				
Wavelength (Å)	Element	EP (eV)	log *gf*	B006	B063	B171	B311	B472
5324.191	26.0	3.211	−0.103	…	…	…	110.9	…
5367.476	26.0	4.420	0.443	…	…	140.4	…	93.3
5369.974	26.0	4.371	0.536	…	…	…	69.4	…
5383.380	26.0	4.312	0.645	…	…	…	73.3	114.0
5389.486	26.0	4.42	−0.410	73.0	59.3	100.7	…	44.8
5393.176	26.0	3.240	−0.715	…	114.1	…	…	105.1
5405.785	26.0	0.990	−1.852	…	…	…	125.0	…
5424.080	26.0	4.320	0.520	…	109.8	…	…	102.8
5429.706	26.0	0.958	−1.881	…	…	…	149.2	…

(This table is available in its entirety in machine-readable form.)

DAGH was funded by the Ramón y Cajal fellowship number RYC-2013-14182 and he acknowledges support provided by the Spanish Ministry of Economy and Competitiveness (MINECO) under grant AYA-2014-58082-P. JS acknowledges partial support from NSF grant AST-1514763 and the Packard Foundation.

APPENDIX
NEW OPTICAL ABUNDANCES FOR FIVE M31 CLUSTERS

In addition to the *H*-band data presented in this paper, optical abundances are derived for five additional clusters. These data supplement the literature data from Colucci et al. (2009, 2014).

A.1. Observations and Data Reduction

The new optical spectra were obtained in 2009 and 2010 with the High Resolution Spectrograph (Tull 1998) on the Hobby–Eberly Telescope (Ramsey et al. 1998; Shetrone et al. 2007) at McDonald Observatory in Fort Davis, TX; details are shown in Table 7. The observations and data reduction were carried out in the same way as the M31 targets in Sakari et al. (2015). Briefly, the 1″ slit was used, yielding a spectral resolution of $R = 30{,}000$. The $600\,{\rm gr\,mm^{-1}}$ cross disperser was positioned to allow spectral coverage over ∼5320–6290 and ∼6360–7340 Å in the blue and the red, respectively. The large 3″ fibers were used to cover the GCs past their half-light radii; fibers located 10″ from the central fiber provided simultaneous sky and background observations, which were subtracted during the data reduction. Hot stellar standards were also observed for removal of telluric features.

The data were reduced in IRAF, utilizing variance weighting during spectral extraction. Normalizations were performed utilizing continuum fits to an extremely metal-poor star, with additional low-order polynomial fits (see Sakari et al. 2013). Individual stellar spectra were cross-correlated with a high-resolution Arcturus spectrum (Hinkle et al. 2003) and shifted to the rest frame. The individual observations were combined with average sigma-clipping, weighted by flux. Velocity dispersions were then determined from a final cross-correlation with Arcturus, as described in Sakari et al. (2013).

A.2. Best-fitting Isochrones

Several of these clusters have been partially resolved with *HST*, allowing constraints to be placed on age and metallicity. However, these CMDs cannot resolve the inner regions, nor do they reach the main sequence turnoff. As in McWilliam & Bernstein (2008), Colucci et al. (2009, 2011, 2014), and Sakari et al. (2015), appropriate isochrone parameters can be determined spectroscopically by minimizing line-to-line trends in Fe I abundance with wavelength, REW, and EP. As

Table 9
Optical Abundances

Element	B006		B063		B171		B311		B472	
	Abundance	*N*	Abundance	*N*	Abundance	*N*	Abundance	*N*	Abundance	*N*
[Fe I/H]	−0.73 ± 0.02	39	−1.10 ± 0.02	35	−0.53 ± 0.02	37	−1.79 ± 0.04	21	−1.17 ± 0.03	48
[Fe II/H]	−0.68 ± 0.14	3	−1.25 ± 0.03	2	−0.57 ± 0.04	3	−1.63 ± 0.04	2	−1.22 ± 0.15	1
[Na I/Fe I]	0.42 ± 0.11	2	0.43 ± 0.13	2	0.64 ± 0.16	2	0.51 ± 0.20	1	⋯	⋯
[Mg I/Fe I]	0.46 ± 0.10	1	0.38 ± 0.09	2	0.32 ± 0.15	1	0.02 ± 0.12	2	0.09 ± 0.09	2
[Al I/Fe I]	0.56 ± 0.13	2	0.44 ± 0.15	1	0.54 ± 0.09	2	⋯		0.74 ± 0.15	1
[Si I/Fe I]	0.46 ± 0.05	2	⋯		0.31 ± 0.07	4	0.37 ± 0.10	2	0.09 ± 0.13	2
[Ca I/Fe I]	0.26 ± 0.02	4	0.42 ± 0.05	4	0.38 ± 0.10	3	0.28 ± 0.05	7	0.28 ± 0.06	6
[Ti I/Fe I]	0.17 ± 0.05	4	0.24 ± 0.03	2	0.29 ± 0.13	3	0.25 ± 0.10	1	⋯	⋯
[Ti II/Fe II]	0.45 ± 0.18	2	0.23 ± 0.10	1	0.34 ± 0.06	2	0.26 ± 0.08	1	0.45 ± 0.04	2
[Ni I/Fe I]	0.02 ± 0.05	6	−0.11 ± 0.03	4	−0.09 ± 0.07	5	−0.23 ± 0.08	2	−0.19 ± 0.18	3
[Ba II/Fe II]	0.31 ± 0.10	2	0.15 ± 0.13	2	−0.40 ± 0.20	2	⋯		−0.19 ± 0.18	2
[Eu II/Fe II]	0.64 ± 0.15	1	0.40 ± 0.25	1	0.33 ± 0.35	1	⋯		0.67 ± 0.15	1

described in Section 3.2, BaSTI isochrones are utilized, since they model the evolved HB and AGB stars. The parameters of the spectroscopically derived isochrones are shown in Table 7, and the values agree well with the literature values.

A.3. Detailed Abundances

The abundances of elements with clean, unblended lines were determined through equivalent width (EW) analyses. This includes Fe, Si, Ca, Ti, and Ni. EWs were measured with the automated program `DAOSPEC` (Stetson & Pancino 2008; also see Sakari et al. 2013) and are provided in Table 8. Abundances were calculated with the IL EW analysis task *abpop* (in the June 2014 version of the code `MOOG`) and are shown in Table 9. Errors are calculated as in Shetrone et al. (2003) and Sakari et al. (2015).

The abundances of the other elements were derived from spectrum syntheses with `MOOG`'s *synpop* routine (see Section 3.1). Abundances of Na, Mg, and Eu were determined with the complete line lists from Sakari et al. (2013). Additionally, Ba and Al lines were synthesized with new line lists that include atomic lines, isotopic information, hyperfine structure, and molecular lines, where appropriate. The best fits were identified by eye, accounting for uncertainties in line profiles and continuum placement.

As in Sakari et al. (2013, 2014, 2015), all optical [Fe/H] and [X/Fe] ratios are calculated differentially, line by line, relative to the solar abundances derived with the same techniques. Three of the targets overlap with Colucci et al. (2014), and the values are generally in good agreement.

REFERENCES

Alvarez, R., & Plez, B. 1998, A&A, 330, 1109

Asplund, M., Grevesse, N., Sauval, J. A., & Scott, P. 2009, ARA&A, 47, 481

Barmby, P., McLaughlin, D. E., Harris, W. E., Harris, G. L. H., & Forbes, D. A. 2007, AJ, 133, 2764

Bergemann, M. 2011, MNRAS, 413, 2184

Briley, M. M., Harbeck, D., Smith, G. H., & Grebel, E. K. 2004, AJ, 127, 1588

Caldwell, N., Harding, P., Morrison, H., et al. 2009, AJ, 137, 94

Caldwell, N., Schiavon, R., Morrison, H., Rose, J. A., & Harding, P. 2011, AJ, 141, 61

Carretta, E., Bragaglia, A., Gratton, R., et al. 2009a, A&A, 505, 117

Carretta, E., Bragaglia, A., Gratton, R., & Lucatello, S. 2009b, A&A, 505, 139

Carretta, E., Bragaglia, A., Gratton, R. P., et al. 2010a, A&A, 516, 55

Carretta, E., Gratton, R. G., Lucatello, S., et al. 2010b, ApJL, 722, L1

Castelli, F., & Kurucz, R. L. 2004, in IAU Symp. 210, Modelling of Stellar Atmospheres, ed. N. Piskunov, W. W. Weiss, & D. F. Gray (San Francisco: ASP), A20

Colucci, J. E., Bernstein, R. A., Cameron, S., McWilliam, A., & Cohen, J. G. 2009, ApJ, 704, 385

Colucci, J. E., Bernstein, R. A., Cameron, S. A., & McWilliam, A. 2011, ApJ, 735, 55

Colucci, J. E., Bernstein, R. A., Cameron, S. A., & McWilliam, A. 2012, ApJ, 746, 29

Colucci, J. E., Bernstein, R. B., & Cohen, J. G. 2014, ApJ, 797, 116

Colucci, J. E., Duran, M. F., Bernstein, R. A., & McWilliam, A. 2013, ApJ, 773, 36

Cordier, D., Pietrinferni, A., Cassisi, S., & Salaris, M. 2007, AJ, 133, 468

Ferguson, J. W., Alexander, D. R., Allard, F., et al. 2005, ApJ, 623, 585

Galleti, S., Bellazzini, M., Buzzoni, A., Federici, L., & Fusi Pecci, F. 2009, A&A, 508, 1285

García-Hernández, D. A., Mészáros, S., Monelli, M., et al. 2015, ApJL, 815, L4

García-Pérez, A. E., Allende Prieto, C., Holtzman, J. A., et al. 2016, AJ, 151, 144

Gratton, R. G., Sneden, C., Carretta, E., & Bragaglia, A. 2000, A&A, 354, 169

Graves, G. J., & Schiavon, R. P. 2008, ApJS, 177, 446

Gunn, J. E., Siegmund, W. A., Mannery, E. J., et al. 2006, AJ, 131, 2332

Hinkle, K., Wallace, L., Livingston, W., et al. 2003, in The Future of Cool-Star Astrophysics: 12th Cambridge Workshop on Cool Stars, Stellar Systems, and the Sun, ed. A. Brown, G. M. Harper, & T. R. Ayres (Boulder, CO: Univ. Colorado), 851

Hogg, D. W., Casey, A. R., Ness, M., Rix, H.-W., & Foreman-Mackey, D. 2016, arXiv:1601.05413

Kraft, R. P, & Ivans, I. I. 2003, PASP, 115, 143

Kroupa, P. 2002, Sci, 295, 82

Lamb, M. P., Venn, K. A., Shetrone, M. D., Sakari, C. M., & Pritzl, B. J. 2015, MNRAS, 448, 42

Lapenna, E., Mucciarelli, A., Ferraro, F. R., et al. 2015, ApJ, 813, 97

Mackey, A. D., Huxor, A. P., Ferguson, A. M. N., et al. 2013, MNRAS, 429, 281

Majewski, S. R., Schiavon, R. P., Frinchaboy, P. M., et al. 2015, arXiv:1509.05420

McWilliam, A., & Bernstein, R. 2008, ApJ, 684, 326

McWilliam, A., Preston, G. W., Sneden, C., & Searle, L. 1995, AJ, 109, 2757

Meszaros, S., Martell, S. L., Shetrone, M., et al. 2015, AJ, 149, 153

Nidever, D. L., Holtzman, J., Allende-Prieto, C., et al. 2015, AJ, 150, 173

Perina, S., Federici, L., Bellazzini, M., Cacciari, C., Fusi Pecci, F., & Galleti, S. 2009, A&A, 507, 1375

Perrett, K. M., Bridges, T. J., Hanes, D. A., et al. 2002, AJ, 123, 2490

Pietrinferni, A., Cassisi, S., Salaris, M., & Castelli, F. 2004, ApJ, 612, 168

Plez, B. 2012, Turbospectrum: Code for spectral synthesis, Astrophysics Source Code Library, ascl:1205.004

Puzia, T. H., & Sharina, M. E. 2008, ApJ, 674, 909

Ramsey, L. W., Adams, M. T., Barnes, T. G., et al. 1998, Proc. SPIE, 3352, 34

Reddy, B. E., Lambert, D. L., & Prieto, C. A. 2006, MNRAS, 367, 1329

Sakari, C. M., Shetrone, M., Venn, K., McWilliam, A., & Dotter, A. 2013, MNRAS, 434, 358

Sakari, C. M., Venn, K., Shetrone, M., Dotter, A., & Mackey, D. 2014, MNRAS, 443, 2285

Sakari, C. M., Venn, K. A., Mackey, D., et al. 2015, MNRAS, 448, 1314

Schiavon, R. P. 2007, ApJS, 171, 146

Schiavon, R. P., Caldwell, N., Conroy, C., et al. 2013, ApJ, 776, 7

Schiavon, R. P., Caldwell, N., Morrison, H., et al. 2012, AJ, 143, 14

Schiavon, R. P., Rose, J. A., Courteau, S., & MacArthur, L. A. 2004, ApJ, 608, 33

Shetrone, M., Bizyaev, D., Lawler, J., et al. 2015, ApJS, 221, 24S

Shetrone, M., Venn, K., Tolstory, E., et al. 2003, AJ, 125, 684

Shetrone, M. D., Cornell, M. E., Fowler, J. R., et al. 2007, PASP, 119, 556

Skrutskie, M. F., Cutri, R. M., Stiening, R., et al. 2006, AJ, 131, 1163

Smith, V. V., Cunha, K., Shetrone, M. D., et al. 2013, ApJ, 765, 16

Sneden, C. 1973, ApJ, 184, 839

Sneden, C., Kraft, R. P., Shetrone, M. D., et al. 1997, AJ, 114, 1964

Stetson, P. B., & Pancino, E. 2008, PASP, 120, 1332

Tolstoy, E., Hill, V., & Tosi, M. 2009, ARA&A, 47, 371

Tripicco, M. J., & Bell, R. A. 1995, AJ, 110, 3035

Tull, R. G. 1998, Proc. SPIE, 3355, 387

VandenBerg, D. A., Bergbusch, P. A., Dotter, A., et al. 2012, ApJ, 755, 15

Venn, K. A., Irwin, M., Shetrone, M. D., et al. 2004, AJ, 128, 1177

Wilson, J. C., Hearty, F., Skrutskie, M. F., et al. 2010, Proc. SPIE, 7735, 77351C

Wilson, John C., Hearty, F., Skrutskie, M. F., et al. 2012, Proc. SPIE, 8446, 8446OH

Worthey, G., Faber, S. M., González, J. J., & Burstein, D. 1994, ApJS, 94, 687

Zasowski, G., Johnson, J. A., Frinchaboy, P. M., et al. AJ, 146, 81

Zhang, H. W., Gehren, T., Butler, K., Shi, J. R., & Zhao, G. 2006, A&A, 457, 645